J. Mech. Phys. Solids 160 (2022) 104739

Contents lists available at ScienceDirect

Journal of the Mechanics and Physics of Solids

journal homepage: www.elsevier.com/locate/jmps

A Kirchhoff-like theory for hard magnetic rods under geometrically nonlinear deformation in three dimensions

Tomohiko G. Sano[1], Matteo Pezzulla[2], Pedro M. Reis *

Flexible Structures Laboratory, Institute of Mechanical Engineering, École Polytechnique Fédérale de Lausanne, Switzerland

ARTICLE INFO

Keywords:
Magnetorheological elastomer
Kirchhoff rod theory
Slender structures
Buckling

ABSTRACT

Magneto-rheological elastomers (MREs) are functional materials that can be actuated by applying an external magnetic field. MREs comprise a composite of hard magnetic particles dispersed into a nonmagnetic elastomeric (soft) matrix. *Hard* MREs have been receiving particular attention because the programmed magnetization remains unchanged upon actuation. Motivated by a new realm of applications, there have been significant theoretical developments in the continuum (three-dimensional) description of hard MREs. In this paper, we derive an effective theory for MRE rods (slender, mono-dimensional structures) under geometrically nonlinear deformation in three dimensions. Our theory is based on reducing the three-dimensional magneto-elastic energy functional for the hard MREs into an one-dimensional Kirchhoff-like description (centerline-based). Restricting the theory to two dimensions, we reproduce previous works on planar deformations. For further validation in the general case of three-dimensional deformation, we perform precision experiments with both naturally straight and curved rods under either constant or constant-gradient magnetic fields. Our theoretical predictions are in excellent agreement with both discrete simulations and precision-model experiments. Finally, we discuss some limitations of our framework, as highlighted by the experiments, where long-range dipole–dipole interactions, which are neglected in the theory, can play a role.

1. Introduction

Leveraging the coupling between internal degrees of freedom and material strains to open up new avenues for structural instabilities has been receiving much recent attention in the mechanics and advanced functional material communities (Li et al., 2009; Dorfmann and Ogden, 2014). The magneto-elastic coupling is particularly interesting since it can be exploited to actuate soft magnetic structures without any mechanical contact. Magneto-rheological elastomers (MREs) comprise a composite of magnetized (metal) particles and a soft elastic matrix that can respond to an applied magnetic field. MREs have long been studied, from both mathematical modeling and application perspectives (Dorfmann and Ogden, 2014; Menzel, 2019). For instance, tunable mechanical functionalities of magnetic structures have been used in the applications such as sensing medical devices (Li et al., 2009), engine mounts (Ginder et al., 1999), soft robotics (Huang et al., 2016), actuators (Hu et al., 2018a), and minimally invasive procedures (Pancaldi et al., 2020).

* Corresponding author.
E-mail address: pedro.reis@epfl.ch (P.M. Reis).
[1] Current affiliation: Laboratory for Structural Instabilities in Geometry and Materials, Department of Mechanical Engineering, Keio University, 3-14-1 Hiyoshi, Kohoku-ku, Yokohama, Kanagawa, 223-8522, Japan.
[2] Current affiliation: Slender Structures Lab, Department of Mechanical and Production Engineering, Århus University, Inge Lehmanns Gade 10, 8000 Århus C, Denmark.

https://doi.org/10.1016/j.jmps.2021.104739
Received 1 July 2021; Received in revised form 18 October 2021; Accepted 2 December 2021
Available online 22 December 2021
0022-5096/© 2022 The Authors. Published by Elsevier Ltd. This is an open access article under the CC BY-NC-ND license (http://creativecommons.org/licenses/by-nc-nd/4.0/).

The mechanical response of MREs to an applied field can be categorized into the following cases, depending on their ingredients, such as the coercivity, which is the necessary field strength to erase the magnetization; (i) *Super-paramagnetic* and *soft-ferromagnetic materials* have large magnetic susceptibility, enabling the temporary magnetization by an external magnetic field (Moon and Pao, 1968; Cebers, 2003; Cēbers and Javaitis, 2004; Dreyfus et al., 2005; Roper et al., 2006; Cēbers and Cīrulis, 2007; Gerbal et al., 2015); a super-paramagnetic material loses its magnetization, once the external field is removed. As a result, the magnetization of these materials depends strongly on the external fields. (ii) *Hard-ferromagnetic materials* have a high coercivity. An external field does not change the magnetization within the range of practical actuation. Hence, their magnetization is independent of external fields. (iii) *Chains of hard-ferromagnetic spheres* are purely magnetic systems without elasticity (Hall et al., 2013; Vella et al., 2014; Schönke and Fried, 2017). The complex internal interaction among beads yields a variety of equilibrium configurations. Interestingly, these chains possess an effective bending stiffness (Vella et al., 2014). (iv) *MREs embedded with soft-ferromagnetic particles* or *soft magnetic elastomer* (Rigbi and Jilkén, 1983; Ginder et al., 1999; Dorfmann and Ogden, 2003; Li et al., 2009; Danas et al., 2012; Loukaides et al., 2015; Seffen and Vidoli, 2016; Schmauch et al., 2017; Ciambella et al., 2018; Singh and Onck, 2018; Psarra et al., 2019; Alapan et al., 2020) deform upon the application of an external magnetic field due to magneto-elastic couplings. The magnetic particles with low coercivity dispersed in a soft matrix align themselves with the applied field, thereby forming particle chains. To enhance the magneto-elastic coupling, it is common to apply the magnetic field to MRE during the curing processes. (v) *MREs embedded with hard-ferromagnetic particles* or *hard magnetic elastomer* have both high coercivity and flexibility in shape-programming (Lum et al., 2016; Kim et al., 2018; Zhao et al., 2019; Wang et al., 2020; Ciambella and Tomassetti, 2020; Chen et al., 2021; Yan et al., 2021b,?; Pancaldi et al., 2020). Once they are saturated magnetically, they retain permanent magnetization. For the remainder of this paper, we will focus on this latter type (v).

The high coercivity of hard MREs enables the design of highly functional mechanical systems, such as auxetic metamaterials (Kim et al., 2018), programmable materials (Chen et al., 2021), micro-swimmers (Diller et al., 2014; Hu et al., 2018b; Zhang and Diller, 2018), micro or soft-robotics (Huang et al., 2016; Tsumori et al., 2015; Hu et al., 2018a) and haptic devices (Pece et al., 2017). Motivated by these emerging applications of hard MREs, it is timely to formulate structural theories for elementary building blocks made of hard MREs to serve as predictive tools in the design process and aid in subsequent analysis.

During the past decade, there have been significant developments in the fundamental theory of hard magnetic elastomers. In a recent pioneering work by Zhao et al. (2019), a nonlinear theory for finite deformation of three-dimensional (bulk) hard MRE was developed, based on the nonlinear elasticity complemented by the magneto-mechanical constitutive laws. In this framework, the Helmholtz free energy density function comprises elastic (neo-Hookean) and magneto-elastic parts. The relationship between the induced magnetic flux density in the material and the external field strength is assumed to be linear, with a permeability close to that of vacuum. The free energy density for the magneto-elastic part is modeled such that the magnetic moment is embedded in a soft matrix. A simulation framework using the finite element method developed by the same authors, based on nonlinear elasticity in three dimensions, was shown to be in quantitative agreement with their experimental results (Zhao et al., 2019).

Based on the framework reported in Zhao et al. (2019), theories for hard magnetic linear beams and elastica have been derived and validated against experiments under either constant magnetic field (Wang et al., 2020) or a field with constant gradient (Yan et al., 2021). Furthermore, it was shown how a hard magnetic beam (or elastica) can buckle under an applied field, analogous to an elastica under compression (Wang, 1986; Lum et al., 2016; Ciambella and Tomassetti, 2020; Wang et al., 2020; Yan et al., 2021). Methodologically, the derivations of all of the above reduced models for hard magnetic linear beam and elastica always boils down to the formal procedure of dimensional reduction (Dill, 1992; Audoly and Pomeau, 2010), which is summarized next. More specifically, the total energy functional of a beam is modeled as Zhao et al. (2019), with elastic and magneto-elastic parts. The integrand is expanded with respect to the thickness of the cross-section, only retaining the leading order terms. Upon integration over the cross-section, a reduced energy is derived. The reduced framework is consistent with the analogous procedure based on force and moment balance (Lum et al., 2016), which was also implemented in the study of the inverse problem (Ciambella and Tomassetti, 2020). A similar strategy based on dimensional reduction has also been employed to predict the axisymmetric deformation of pressurized hard magnetic shells (Yan et al., 2021b).

While theoretical frameworks for one-dimensional hard magnetic slender structures are now well established for planar deformations (e.g., beams and elastica), the modeling of hard magnetic rods, with natural curvatures, undergoing three-dimensional deformation is still lacking. However, the extension of the formulation in two dimensions toward three-dimensional deformation is not straightforward because of the complex interplay between elasticity and geometry (Dill, 1992; Audoly and Pomeau, 2010; Landau and Lifshitz, 1980; Powers, 2010; Bigoni, 2015; Goriely, 2017). The precise modeling of a *hard magnetic elastomeric rod* is crucial to simulate, for example, micro-magnetic-swimmers (Diller et al., 2014; Hu et al., 2018b; Zhang and Diller, 2018) in a complex channel, and endovascular probes (Pancaldi et al., 2020).

In this paper, we establish a theory for the deformation of *hard magnetic elastomeric rods*, combining dimensional reduction and simulations, both of which are validated against precision experiments. For our theory, we start from the total energy functional comprising the sum of the Hookean elastic energy (Audoly and Pomeau, 2010) and the magneto-elastic free-energy proposed in Zhao et al. (2019). We then employ the centerline-based kinematics utilizing the Cosserat frame and Darboux vector (Goriely, 2017). Along the (circular) cross-section, we span the (local) polar coordinate around the centerline position to parametrize the material points of the hard magnetic rod. Subsequently, we expand the integrand of the magneto-elastic energy in the rod diameter, retaining only the leading order terms. After integrating the integrand over the cross-section, we obtain the reduced magneto-elastic functional. Based on this reduced magneto-elastic functional, we then apply the principle of virtual work to arrive at the governing nonlinear ordinary differential equations (strong form of the problem). The derived equilibrium equations are analogous to the Kirchhoff rod equations, but with additional magneto-elastic terms; hence, we call them the *magnetic Kirchhoff rod equations*. The nonlinear deformations

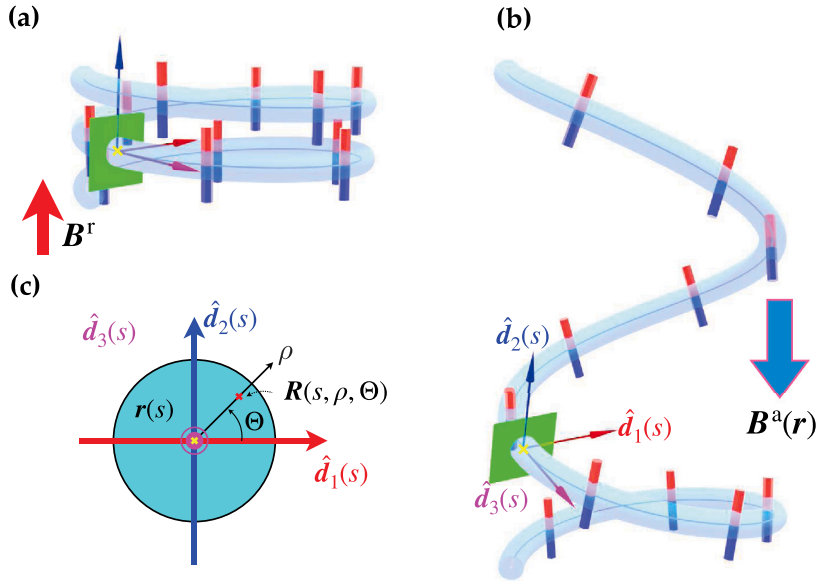

Fig. 1. Definition of the problem. (a) A naturally curved and twisted rod is magnetized permanently along $\boldsymbol{B}^{\mathrm{r}}$. (b) Subsequently, when a magnetic field $\boldsymbol{B}^{\mathrm{a}}$ is applied, the rod deforms due to the induced magnetic force and torque. The centerline of the rod is described uniquely by the rotation of the Cosserat frame $(\hat{\boldsymbol{d}}_1, \hat{\boldsymbol{d}}_2, \hat{\boldsymbol{d}}_3)$ along the arc-length s. (c) The cross section of the rod is assumed circular. Any material point of the three-dimensional rod is identified by the cylindrical coordinates (s, ρ, Θ), where polar coordinates (ρ, Θ) are set on the $\hat{\boldsymbol{d}}_1 - \hat{\boldsymbol{d}}_2$ plane for each value of s.

based on the magnetic Kirchhoff rod equations are computed with the discrete simulation method (Chirico and Langowski, 1994; Wada and Netz, 2007b,a; Vogel and Stark, 2010; Reichert, 2006; Bergou et al., 2008; Morigaki et al., 2016; Sano et al., 2017; Sano and Wada, 2018, 2019). Both the dimensional reduction procedure and the simulations are then validated against precision experiments. Since our theory is based on the assumption that the magnetic torque is induced by the misalignment between the magnetization and the applied field, the long-range dipole interactions are not modeled. Still, we find excellent agreement between theory and experiments as long as the long-range dipole interactions are negligible. We quantify when and how the long-range interactions become important in the experiments.

Very recently, a Kirchhoff-like theory for paramagnetic rods was proposed in Barreto et al. (2021). Based on the dimensional reduction, similarly to the procedure that we will follow in our study, the force and moment balance equations along the centerline were derived, but without experimental validation like in our case. Given that paramagnetic rods do not possess a residual flux density, the theory developed in Barreto et al. (2021) is rooted in the different magneto-elastic interaction potential than the one we use for hard-magnetic materials. Thus, our theoretical framework, which will be validated experimentally, is distinct from that in Barreto et al. (2021).

Our paper is organized as follows. In Section 2, we define the problem. The derivation of the magnetic Kirchhoff equations follows in Section 3, where we also show that our theory reproduces the previous results of planar deformation of hard magnetic elastica and beams. To compute geometrically nonlinear deformation in three dimensions, we numerically solve the derived set of equations as detailed in Section 4. In Section 5, the experimental fabrication, apparatus, and protocols are presented. We report the comparison between theory and experiment in Section 6. We further discuss the limitation of our theory systematically in Section 7. In Section 8, we discuss and summarize our findings.

2. Definition of the problem

In this section, we define the problem and identify the relevant variables. We consider a naturally curved and twisted (inextensible) rod of circular cross-section with diameter d (area $A = \pi d^2/4$) and total length L (Fig. 1(a)) (Landau and Lifshitz, 1980; Powers, 2010; Audoly and Pomeau, 2010; Bigoni, 2015; Goriely, 2017). The goal of our study was to derive a reduced-order theoretical framework to describe the deformation of the centerline, $\boldsymbol{r}(s)$, of this hard magnetic rod, upon magnetic actuation. The arc-length of the centerline is s ($0 \le s \le L$). In particular, we seek to derive the set of governing ordinary differential equations (ODEs); i.e., the strong form of the problem depicting force and moment balance of the system. This section details the kinematics and constitutive relations of our system, in Sections 2.1 and 2.2, respectively.

2.1. Kinematics

Our rod is slender such that the diameter is significantly smaller than its length; $d/L \ll 1$. Throughout this paper, we denote the quantities in the reference configuration with $\mathring{(\cdot)}$. For example, we write the centerline position in the reference configuration

as $\mathring{\boldsymbol{r}}(s)$. The vectors $(\hat{\boldsymbol{d}}_1, \hat{\boldsymbol{d}}_2, \hat{\boldsymbol{d}}_3)$ form a local orthonormal basis attached to every point on the rod's centerline. Here, the first two vectors lie in the deformed cross-sectional plane while the third one $\hat{\boldsymbol{d}}_3$ is aligned with the cross-section normal and also equals the centerline tangent, $\boldsymbol{r}'$; $\hat{\boldsymbol{d}}_3 = \boldsymbol{r}'(s)$. Here $(\cdot)'$ represents differentiation with respect to s. With the help of the Cosserat frame basis $\hat{\boldsymbol{d}}_a$ $(a = 1, 2, 3)$ defined here, one can uniquely identify the configuration of the rod centerline (other than rigid body translations and rotations). The rotation of the Cosserat frame can be represented using the Darboux vector $\boldsymbol{\Omega} = \Omega_a \hat{\boldsymbol{d}}_a$ as

$$\hat{\boldsymbol{d}}_a' = \boldsymbol{\Omega} \times \hat{\boldsymbol{d}}_a, \tag{1}$$

where Ω_a are the rotation rates of the Cosserat frame around $\hat{\boldsymbol{d}}_a$ (Landau and Lifshitz, 1980; Powers, 2010; Audoly and Pomeau, 2010; Bigoni, 2015; Goriely, 2017). We can then define the slenderness parameters as $\mathring{\Omega}_a d$.

The three-dimensional reference configuration of the rod can be described uniquely by introducing the cylindrical coordinates $\xi_\mu = s, \rho, \Theta$ $(0 \le \rho \le d/2,\ 0 \le \Theta \le 2\pi)$, whose origin corresponds to $\boldsymbol{r}(s)$ as shown in Fig. 1(c). For example, the position vector of the rod-body is

$$\boldsymbol{R}(s, \rho, \Theta) = \boldsymbol{r}(s) + \rho \cos\Theta\ \hat{\boldsymbol{d}}_1(s) + \rho \sin\Theta\ \hat{\boldsymbol{d}}_2(s). \tag{2}$$

Once the geometry is set up, we can obtain information about the deformation of the three-dimensional body, which is characterized by the deformation gradient $\mathbf{F}$, defined as

$$\mathbf{F} \equiv \frac{\partial \boldsymbol{R}}{\partial \mathring{\boldsymbol{R}}} = \boldsymbol{t}_\mu \otimes \mathring{\boldsymbol{t}}^\dagger_\mu. \tag{3}$$

The tangent vector $\boldsymbol{t}_\mu$ along the curvilinear coordinate μ, is expressed as $\boldsymbol{t}_\mu = \partial \boldsymbol{R}/\partial \xi_\mu$, where $\xi_\mu = s, \rho, \Theta$ for $\mu = 1, 2, 3$, respectively. The reciprocal basis of $\boldsymbol{t}_\mu$ denoted by, $\boldsymbol{t}^\dagger_\mu$, is defined as $\boldsymbol{t}^\dagger_\mu \cdot \boldsymbol{t}_\nu = \delta_{\mu\nu}$ with the Kronecker delta $\delta_{\mu\nu}$, which is equivalently written as $\boldsymbol{t}^\dagger_\mu \equiv \partial \xi_\mu / \partial \boldsymbol{R}$. By using the kinematic relations, we can calculate the tangent vectors. Note, for example, that when $\mathring{\boldsymbol{t}}^\dagger_\mu$ and $\boldsymbol{t}_\mu$ are expressed in terms of the Cartesian basis $(\hat{\boldsymbol{e}}_x, \hat{\boldsymbol{e}}_y, \hat{\boldsymbol{e}}_z)$, each component of $\mathbf{F}$ is calculated as $F_{ij} = (\boldsymbol{t}_\mu \cdot \hat{\boldsymbol{e}}_i)(\mathring{\boldsymbol{t}}^\dagger_\mu \cdot \hat{\boldsymbol{e}}_j)$ $(i, j = x, y, z)$. Throughout this paper, a, b, c and i, j, k are indices of the Cosserat frame and the Cartesian basis, respectively, unless specified otherwise.

2.2. Constitutive relation and magneto-elastic potential

We assume that the rod is made of a Hookean material, where the internal stress is linearly proportional to the strain (Audoly and Pomeau, 2010). The rod is permanently magnetized in the reference configuration with a magnetic flux density $\boldsymbol{B}^{\mathrm{r}}$. We investigate the deformation of the rod upon the application of an external applied magnetic flux density vector $\boldsymbol{B}^{\mathrm{a}}(\boldsymbol{r})$ (Fig. 1(b)). Note that the applied field $\boldsymbol{B}^{\mathrm{a}}$ is set to vary in space. We will specialize our theory in the cases of either homogeneous $\partial \boldsymbol{B}^{\mathrm{a}}/\partial r_i = 0$ or inhomogeneous fields $\partial \boldsymbol{B}^{\mathrm{a}}/\partial r_i \neq 0$, making use of the precision experimental framework introduced in Section 5.2.

As a starting point for the derivation of our Kirchhoff-like theory for hard magnetic rods, we will make use of the Helmholtz free energy for ideal hard-magnetic soft materials that was introduced recently in Kim et al. (2018), Zhao et al. (2019); which we review next. Once the rod is magnetized, all magnetized moments are parallel with $\boldsymbol{B}^{\mathrm{r}}$ (fully saturated). Hence, it is reasonable to assume that the magnetic permeability of the hard magnetic material is close to that of vacuum μ_0. The magnetized moments will not affect the (surrounding) applied field $\boldsymbol{B}^{\mathrm{a}}$ upon actuation. Besides, the permeability of the elastomer that we will use in the experiments (Section 5.2) is nearly the same as that of the vacuum μ_0. The magnetization density vector per unit volume in the deformed configuration is modeled as the transformation of $\boldsymbol{B}^{\mathrm{r}}$ as $\boldsymbol{\mathcal{M}}_{3\mathrm{D}} = \mathbf{F}\boldsymbol{B}^{\mathrm{r}}/\mu_0$. Thus, the total magneto-elastic energy for a hard magnetic rod can be simplified as the work to align the residual magnetic moment of the material with $\boldsymbol{B}^{a}$:

$$E_{\mathrm{mag}} = -\iiint \boldsymbol{\mathcal{M}}_{3\mathrm{D}} \cdot \boldsymbol{B}^{\mathrm{a}} \rho d\rho d\Theta ds = -\iiint \frac{1}{\mu_0} (\mathbf{F}\boldsymbol{B}^{\mathrm{r}}) \cdot \boldsymbol{B}^{\mathrm{a}} \rho d\rho d\Theta ds\,. \tag{4}$$

Note here that we do not consider the internal stress or long-range forces induced by a dipole–dipole interaction (Hall et al., 2013; Jackson, 1975; Vella et al., 2014; Garcia-Gonzalez and Hossain, 2021). The validity of this simplifying assumption will be evaluated thoroughly in Section 7. In the following, by integrating Eq. (4) over the cross-section, we seek to obtain the reduced expression for the magneto-elastic energy density of the rod per unit *length*, up to the leading order in the slenderness parameter.

3. Theory of a Kirchhoff-like equation for hard magnetic elastic rods

In this section, we derive the equilibrium equations (ODEs) describing the geometrically nonlinear deformation of hard magnetic rods. The main results of this section are Eqs. (24) and (25), that are the magnetic Kirchhoff rod equations. To arrive at this set of ODEs, in Section 3.1, we will follow the procedure of dimensional reduction. In Section 3.2, we review the derivation of the *non-magnetic* Kirchhoff rod equations based on the principle of virtual work. We derive the distributed magneto-elastic force $\boldsymbol{p}_{\mathrm{mag}}$ and torque $\boldsymbol{q}_{\mathrm{mag}}$ through variational calculus in Section 3.3, thus obtaining the magnetic Kirchhoff rod equations for hard magnetic rods. In Section 3.4, we show that our framework reproduces previous works on the planar deformation of hard magnetic beams and elastica (Lum et al., 2016; Ciambella and Tomassetti, 2020; Wang et al., 2020; Yan et al., 2021), whereas in Section 6 we will employ our framework to study cases where the deformation is three-dimensional.

3.1. Reduced magneto-elastic and elastic energy

Integrating Eq. (4) over the cross-section will yield the reduced energy of the rod system, to leading order of slenderness parameter $O(1)$ ($\mathring{\Omega}_a d, \Omega_a d \ll 1$). To proceed, we first expand the deformation gradient as

$$\mathbf{F} = \mathbf{D}(s) + \frac{\partial u_\beta}{\partial X_\alpha}\hat{\boldsymbol{d}}_\beta(s) \otimes \mathring{\hat{\boldsymbol{d}}}_\alpha(s) + \{(H_{a\beta} - \mathring{H}_{a\beta})X_\beta\}\hat{\boldsymbol{d}}_a(s) \otimes \mathring{\hat{\boldsymbol{d}}}_3(s) \tag{5}$$

where we define the asymmetric tensor H_{ab}; $H_{ab} = -\varepsilon_{abc}\Omega_c$ with the Eddington epsilon ε_{abc} and the coordinate along $\hat{\boldsymbol{d}}_\alpha$, X_α ($\alpha = 1, 2$). Note that subscript α, β in (5) runs over only 1 and 2. The in-plane displacement along the cross section is denoted by u_α; $u_1 = -\nu(\Omega_1 - \mathring{\Omega}_1)X_1X_2 + \nu(\Omega_2 - \mathring{\Omega}_2)(X_1^2 - X_2^2)/2$, $u_2 = \nu(\Omega_2 - \mathring{\Omega}_2)X_1X_2 + \nu(\Omega_1 - \mathring{\Omega}_1)(X_1^2 - X_2^2)/2$ (Dill, 1992). The second and third terms in (5) provides us the bend and twist deformation of the rod. On the other hand the first term $\mathbf{D}(s)$ represents the $O(1)$ term.

$$\mathbf{D}(s) \equiv \hat{\boldsymbol{d}}_a(s) \otimes \mathring{\hat{\boldsymbol{d}}}_a(s) \tag{6}$$

is the reduced deformation gradient, mapping the undeformed tangent space to the deformed tangent space along the centerline of the rod. Substituting Eq. (5) into Eq. (4), we can reduce the magneto-elastic energy to the one-dimensional integral. We notice that the second and third terms in Eq. (5) are odd functions of X_1 or X_2. The integrand of Eq. (4) is expanded as

$$(\mathbf{F}\boldsymbol{B}^{\mathrm{r}}) \cdot \boldsymbol{B}^{\mathrm{a}}(\boldsymbol{R}) = (\mathbf{D}\boldsymbol{B}^{\mathrm{r}}) \cdot \boldsymbol{B}^{\mathrm{a}}(\boldsymbol{r}) + \mathcal{L}(s, X_1, X_2) + O\left(X_\alpha^2 B^{\mathrm{r}} |\nabla \boldsymbol{B}^{\mathrm{a}}| \mathring{\Omega}_\alpha\right). \tag{7}$$

Here, $\mathcal{L} = \mathcal{L}(s, X_1, X_2)$ represents the sum of linear terms in X_1 and X_2, which vanishes upon integration over the cross section $\int dX_1 dX_2$. We neglect the quadratic terms $O\left(X_\alpha^2 B^{\mathrm{r}} |\nabla \boldsymbol{B}^{\mathrm{a}}| \mathring{\Omega}_\alpha\right)$. These terms would play a role if the magnetic rod is not slender or highly curved, or if $\boldsymbol{B}^{\mathrm{a}}$ varies largely over the cross section. In summary, up to the linear order in X_1 and X_2, the reduced gradient $\mathbf{D}$ only gives the non-zero contribution in Eqs. (4) and (5). Given that $\mathbf{D}$ is not a function of ρ nor Θ, the integral along the cross-section is replaced by the constant cross-section area A. Hence, from Eq. (4), we obtain the reduced magneto-elastic energy functional as

$$E_{\mathrm{mag}} = -\int_0^L \boldsymbol{\mathcal{M}}(s) \cdot \boldsymbol{B}^{\mathrm{a}}(\boldsymbol{r}(s)) ds\,, \tag{8}$$

where we have introduced the magnetization density vector per unit length $\boldsymbol{\mathcal{M}}$ (by contrast to the three-dimensional counterpart, $\boldsymbol{\mathcal{M}}_{3\mathrm{D}}$, introduced above) defined as

$$\boldsymbol{\mathcal{M}}(s) \equiv \frac{A}{\mu_0}(\mathbf{D}(s)\boldsymbol{B}^{\mathrm{r}}). \tag{9}$$

It is important to note that, when the applied field $\boldsymbol{B}^{\mathrm{a}}$ is not uniform, $\boldsymbol{B}^{\mathrm{a}}$ at the material point $\boldsymbol{R}(s, \rho, \Theta)$ is represented by the value at the centerline position $\boldsymbol{r}(s)$ as $\boldsymbol{B}^{\mathrm{a}}(\boldsymbol{R}(s, \rho, \Theta)) \simeq \boldsymbol{B}^{\mathrm{a}}(\boldsymbol{r}(s))$. The spatial variation of $\boldsymbol{B}^{\mathrm{a}}$ along the cross section is at higher order of slenderness parameter $O(\mathring{\Omega}_a d, \Omega_a d)$ as $\boldsymbol{B}^{\mathrm{a}}(\boldsymbol{R}) = \boldsymbol{B}^{\mathrm{a}}(\boldsymbol{r}) + O(\mathring{\Omega}_a d, \Omega_a d)$, and can, therefore, be neglected.

We now want to derive the equilibrium equations, augmenting the (non-magnetic) Kirchhoff rod equations. In the absence of magnetic effects, we recall that, from the literature (Audoly and Pomeau, 2010; Landau and Lifshitz, 1980; Powers, 2010; Bigoni, 2015; Goriely, 2017), the total elastic energy for a naturally curved and twisted elastic (Hookean) rod in the absence of a magnetic field is given by

$$E_{\mathrm{el}} = \int_0^L \frac{EI}{2}\left\{\left(\Omega_1 - \mathring{\Omega}_1\right)^2 + \left(\Omega_2 - \mathring{\Omega}_2\right)^2\right\} + \frac{GJ}{2}\left(\Omega_3 - \mathring{\Omega}_3\right)^2 ds, \tag{10}$$

where EI and GJ are the bending and twist moduli, respectively, with E as the Young modulus, $G = E/\{2(1+\nu)\}$ as the shear modulus with the Poisson ratio ν, $I = \pi d^4/64$ as the second moment of area and $J = \pi d^4/32$ as the torsional constant.

The set of equations of mechanical equilibrium is derived through the principle of virtual work as

$$\delta E_{\mathrm{el}} + \delta E_{\mathrm{mag}} = \delta W_{\mathrm{ex}}, \tag{11}$$

where W_{ex} is the work done by the external forces and torques, $(\boldsymbol{F}_{\mathrm{ex}}(0), \boldsymbol{M}_{\mathrm{ex}}(0))$ and $(\boldsymbol{F}_{\mathrm{ex}}(L), \boldsymbol{M}_{\mathrm{ex}}(L))$, applied at $s = 0$ and $s = L$, respectively, together with the distributed external forces $\boldsymbol{p}(s)$ and torques $\boldsymbol{q}(s)$ per unit length (e.g., gravity, viscous force and torque).

The magnetic Kirchhoff rod equations can be derived directly from Eq. (11), which will be tackled in Section 3.3. Before describing our theory for magnetic rods, we review the well-established (*non-magnetic*) Kirchhoff rod equations. Note that $\delta E_{\mathrm{el}} = \delta W_{\mathrm{ex}}$ corresponds to the case in the absence of the magnetic field. Given that E_{mag} is additive in the total energy, the variation of E_{mag} alone will yield the expressions of the distributed magneto-elastic force $\boldsymbol{p}_{\mathrm{mag}}$ and torque $\boldsymbol{q}_{\mathrm{mag}}$ per unit length, which must be added to the force and moment balance equations as an external force and torque, respectively.

3.2. Review of the (non-magnetic) Kirchhoff rod equations

In the previous section, we have derived the reduced expressions for the magneto-elastic potential. In the absence of the magnetic field $E_{\mathrm{mag}} = 0$, the variations of E_{el} and W_{ex} follow the (non-magnetic) Kirchhoff rod equations. In this section, for completeness, we review their derivation. The Kirchhoff rod equations can be derived by considering the restricted variation of the total energy

functional such that the centerline does not stretch: $\delta(ds) = 0$ (i.e., the differentiation with respect to s, d/ds, and the variation, δ, commute). A detailed account of this derivation can be found in Powers (2010); in what follows, we provide just a brief sketch.

The variation of the elastic energy functional $\delta E_{\rm el}$ is written using the variation of Ω_a, $\delta\Omega_a$:

$$\delta E_{\rm el} = \int_0^L EI(\Omega_1 - \mathring{\Omega}_1)\delta\Omega_1 + EI(\Omega_2 - \mathring{\Omega}_2)\delta\Omega_2 + GJ(\Omega_3 - \mathring{\Omega}_3)\delta\Omega_3 ds. \tag{12}$$

To rewrite Eq. (12) with respect to the angular parameters and infinitesimal angles $\boldsymbol{\epsilon}$ (Powers, 2010), the infinitesimal rotation vector of the Cosserat frame $\boldsymbol{\epsilon}$ is introduced as $\boldsymbol{\epsilon} \equiv \delta\chi_a \hat{\boldsymbol{d}}_a$ whose components are expressed as $\delta\chi_1 \equiv (\delta\hat{\boldsymbol{d}}_2)\cdot\hat{\boldsymbol{d}}_3 = -(\delta\boldsymbol{r})'\cdot\hat{\boldsymbol{d}}_2$, $\delta\chi_2 \equiv (\delta\hat{\boldsymbol{d}}_3)\cdot\hat{\boldsymbol{d}}_1 = (\delta\boldsymbol{r})'\cdot\hat{\boldsymbol{d}}_1$, and $\delta\chi_3 \equiv (\delta\hat{\boldsymbol{d}}_1)\cdot\hat{\boldsymbol{d}}_2 = -(\delta\hat{\boldsymbol{d}}_2)\cdot\hat{\boldsymbol{d}}_1$. Thanks to the infinitesimal rotation vector $\boldsymbol{\epsilon}$, we can simplify Eq. (12) as

$$\delta E_{\rm el} = \boldsymbol{M}(L)\cdot\boldsymbol{\epsilon}(L) - \boldsymbol{M}(0)\cdot\boldsymbol{\epsilon}(0) - \int_0^L \boldsymbol{M}'\cdot\boldsymbol{\epsilon} ds, \tag{13}$$

with the internal moment vector $\boldsymbol{M}(s) = M_a\hat{\boldsymbol{d}}_a = EI\{(\Omega_1 - \mathring{\Omega}_1)\hat{\boldsymbol{d}}_1 + (\Omega_2 - \mathring{\Omega}_2)\hat{\boldsymbol{d}}_2\} + GJ(\Omega_3 - \mathring{\Omega}_3)\hat{\boldsymbol{d}}_3$. The end-forces and moments are applied at $s = 0$ and $s = L$ as $\boldsymbol{F}_{\rm ex}(0), \boldsymbol{M}_{\rm ex}(0), \boldsymbol{F}_{\rm ex}(L)$, and $\boldsymbol{M}_{\rm ex}(L)$, respectively. The rod is subjected to the distributed external force and torque per unit length $\boldsymbol{p}(s)$ and $\boldsymbol{q}(s)$. The variation of the work done by the external forces and torques (in the absence of magnetic fields) is

$$\begin{aligned}\delta W_{\rm ex} &= \boldsymbol{F}_{\rm ex}(0)\cdot\delta\boldsymbol{r}(0) + \boldsymbol{F}_{\rm ex}(L)\cdot\delta\boldsymbol{r}(L) + \boldsymbol{M}_{\rm ex}(0)\cdot\boldsymbol{\epsilon}(0) + \boldsymbol{M}_{\rm ex}(L)\cdot\boldsymbol{\epsilon}(L)\\ &\quad + \int_0^L \{\boldsymbol{p}(s)\cdot\delta\boldsymbol{r}(s) + \boldsymbol{q}(s)\cdot\boldsymbol{\epsilon}(s)\}\, ds.\end{aligned} \tag{14}$$

The internal and external virtual works expressed with respect to $\delta\boldsymbol{r}$ and $\boldsymbol{\epsilon}$ are then equated as $\delta E_{\rm el} = \delta W_{\rm ex}$. Following the convention described in Audoly and Pomeau (2010), the internal force acting over the cross section at s, $\boldsymbol{F}(s)$, is defined by integrating the force from $s = L$;

$$\boldsymbol{F}(s) \equiv \boldsymbol{F}(L) + \int_s^L \boldsymbol{p}(s')ds'. \tag{15}$$

In addition, we rewrite one of the terms in Eq. (14), $\boldsymbol{p}(s)\cdot\delta\boldsymbol{r}$, as $\boldsymbol{p}\cdot\delta\boldsymbol{r} = -(\boldsymbol{F}\cdot\delta\boldsymbol{r})' + \boldsymbol{\epsilon}\cdot(\hat{\boldsymbol{d}}_3\times\boldsymbol{F})$. Collecting the terms associated with $\delta\boldsymbol{r}(s)$ and $\boldsymbol{\epsilon}(s)$ yields the (non-magnetic) Kirchhoff rod equations

$$\boldsymbol{F}'(s) + \boldsymbol{p}(s) = 0, \tag{16}$$

$$\boldsymbol{M}'(s) + \hat{\boldsymbol{d}}_3(s)\times\boldsymbol{F}(s) + \boldsymbol{q}(s) = 0. \tag{17}$$

Eqs. (16) and (17) are the equilibrium equations of forces and moments for the rod, respectively. In parallel with the derivation of Eqs. (16) and (17), the boundary conditions can be also derived from variational calculus (Powers, 2010) as

$$\boldsymbol{M}(0) = -\boldsymbol{M}_{\rm ex}(0), \quad \boldsymbol{M}(L) = \boldsymbol{M}_{\rm ex}(L), \quad \boldsymbol{F}(0) = -\boldsymbol{F}_{\rm ex}(0), \quad \boldsymbol{F}(L) = \boldsymbol{F}_{\rm ex}(L). \tag{18}$$

Next, we will tackle the derivation of the magnetic Kirchhoff rod equations based on the same procedure sketched above, while the elastic terms Eqs. (16) and (17) remain unchanged. The last task is to compute the variation of the magneto-elastic potential, $E_{\rm mag}$, with respect to $\delta\boldsymbol{r}(s)$ and $\boldsymbol{\epsilon}(s)$, $\delta E_{\rm mag}$, which is addressed next.

3.3. Derivation of the magnetic Kirchhoff rod equations using the principle of virtual work

We now set out to derive the magnetic Kirchhoff rod equations. First, we will compute the variation of the magneto-elastic potential, $\delta E_{\rm mag}$. Equating the total internal and external virtual works as Eq. (11), we will obtain the magnetic Kirchhoff rod equations. Given that $\delta E_{\rm el}, \delta W_{\rm ex}$, and $\delta E_{\rm mag}$ are additive in Eq. (11), the variation of the magneto-elastic potential $\delta E_{\rm mag}$ provides the distributed magneto-elastic force $\boldsymbol{p}_{\rm mag}$ and torque $\boldsymbol{q}_{\rm mag}$ explicitly, which will be readily added to Eqs. (16) and (17) to capture magnetic effects.

Before calculating $\delta E_{\rm mag}$, we compute the variation of the Cosserat frame basis $\hat{\boldsymbol{d}}_a$, $\delta\hat{\boldsymbol{d}}_a$. Given that $\boldsymbol{\epsilon}$ represents the infinitesimal rotation around $\hat{\boldsymbol{d}}_a$, the variation of $\hat{\boldsymbol{d}}_a$ is $\delta\hat{\boldsymbol{d}}_a = \boldsymbol{\epsilon}\times\hat{\boldsymbol{d}}_a = -\varepsilon_{abc}\delta\chi_b\hat{\boldsymbol{d}}_c$, where ε_{abc} is the Eddington epsilon. We aim to express $\delta E_{\rm mag}$ with respect to $\delta\boldsymbol{r}$ and $\boldsymbol{\epsilon}$. Note that $\delta\boldsymbol{B}^{\rm r}$ and $\delta\mathring{\hat{\boldsymbol{d}}}_a$ are zero, since they do not depend on the state variables. We first determine the variation of the reduced deformation gradient $\mathbf{D}$ as

$$\begin{aligned}\delta\mathbf{D} &= \delta(\hat{\boldsymbol{d}}_a\otimes\mathring{\hat{\boldsymbol{d}}}_a) = (\boldsymbol{\epsilon}\times\hat{\boldsymbol{d}}_a)\otimes\mathring{\hat{\boldsymbol{d}}}_a\\ &= \mathbf{eD},\end{aligned} \tag{19}$$

where the skew-symmetric tensor $\mathbf{e}$ is formed from $\boldsymbol{\epsilon} = \epsilon_a\hat{\boldsymbol{d}}_a$; $e_{ab} \equiv \varepsilon_{abc}\epsilon_c$ $(a, b = 1, 2, 3)$, with Eddington's epsilon ε_{abc}. Given that the variation of $\boldsymbol{B}^{\rm a}(\boldsymbol{r})$ acts as $\delta\boldsymbol{B}^{\rm a} = (\partial\boldsymbol{B}^{\rm a}/\partial r_i)\delta r_i \equiv (\nabla\boldsymbol{B}^{\rm a})\delta\boldsymbol{r}$, we compute the variation of $E_{\rm mag}$, $\delta E_{\rm mag}$ as

$$\delta E_{\rm mag} = -\int_0^L [\delta\boldsymbol{r}\cdot\boldsymbol{p}_{\rm mag}(s) + \boldsymbol{\epsilon}\cdot\boldsymbol{q}_{\rm mag}(s)]ds, \tag{20}$$

$$\boldsymbol{p}_{\rm mag}(s) \equiv \frac{\Lambda}{\mu_0}(\mathbf{D}(s)\boldsymbol{B}^{\rm r})\cdot(\nabla\boldsymbol{B}^{\rm a}) = \boldsymbol{\mathcal{M}}\cdot(\nabla\boldsymbol{B}^{\rm a}), \tag{21}$$

$$\boldsymbol{q}_{\text{mag}}(s) \equiv \boldsymbol{\mathcal{M}} \times \boldsymbol{B}^{\text{a}}. \tag{22}$$

We have introduced $\boldsymbol{p}_{\text{mag}}$ and $\boldsymbol{q}_{\text{mag}}$ as the distributed magneto-elastic force and torque, respectively. When the applied field is homogeneous $\partial \boldsymbol{B}^{\text{a}}/\partial r_i = 0$, the magnetic torque $\boldsymbol{q}_{\text{mag}} \neq 0$ drives the deformation (i.e., $\boldsymbol{p}_{\text{mag}} = 0$), while both $\boldsymbol{p}_{\text{mag}}$ and $\boldsymbol{q}_{\text{mag}}$ contribute to the deformation if the applied field is inhomogeneous.

Adding the distributed magneto-elastic force and torque terms from Eqs. (21) and (22) into the (non-magnetic) Kirchhoff rod equations (16) and (17), yields the force and moment balance equations. Upon derivation, we need to define the internal force $\boldsymbol{F}(s)$ for hard magnetic rods. Similar to Eq. (15), the internal force $F(s)$ is integral of the distributed external force and magneto-elastic force;

$$\boldsymbol{F}(s) \equiv \boldsymbol{F}(L) + \int_s^L \boldsymbol{p}(s') + \boldsymbol{p}_{\text{mag}}(s') ds'. \tag{23}$$

Hence, the magnetic Kirchhoff rod equations are given by

$$\boldsymbol{F}'(s) + \boldsymbol{p}(s) + \boldsymbol{p}_{\text{mag}}(s) = 0, \tag{24}$$

$$\boldsymbol{M}'(s) + \hat{\boldsymbol{d}}_3(s) \times \boldsymbol{F}(s) + \boldsymbol{q}(s) + \boldsymbol{q}_{\text{mag}}(s) = 0, \tag{25}$$

where the distributed magnetic force $\boldsymbol{p}_{\text{mag}}$ and torque $\boldsymbol{q}_{\text{mag}}$ were defined in Eqs. (21) and (22), respectively. Note that the boundary conditions specified in Eq. (18) remain unchanged in the magneto-elastic case because they do not appear in Eq. (20). We refer to the set of Eqs. (24) and (25) as the *magnetic Kirchhoff rod equations*, where the coupling between elasticity and magnetism is captured by $\boldsymbol{p}_{\text{mag}}$ and $\boldsymbol{q}_{\text{mag}}$.

In Barreto et al. (2021), the magnetic contributions of both the internal force, $\boldsymbol{F}_{\text{m}}$, and the internal moment, $\boldsymbol{M}_{\text{m}}$, are discussed. Whereas the model described in Barreto et al. (2021) is based on a paramagnetic (not hard-magnetic) theory, we will follow a similar argument to determine the magnetic contribution of the internal loads in our case. We define the magneto-elastic energy density, e_{mag}, such that $E_{\text{mag}} = \iiint e_{\text{mag}} dX_1 dX_2 ds$. The first *magnetic* Piola–Kirchhoff tensor $\mathbf{T}_{\text{m}}$ is calculated as $\mathbf{T}_{\text{m}} \equiv \partial e_{\text{mag}}/\partial \mathbf{F} = -\boldsymbol{B}^{\text{a}} \otimes \boldsymbol{\mathcal{M}}_0$, where $\boldsymbol{\mathcal{M}}_0$ represents the magnetization vector in the reference configuration, $\boldsymbol{\mathcal{M}}_0 \equiv \boldsymbol{B}^{\text{r}}/\mu_0$. Using $\mathbf{T}_{\text{m}}$, we compute $\boldsymbol{F}_{\text{m}}$ and $\boldsymbol{M}_{\text{m}}$. Using $\mathbf{T}_{\text{m}}$, we obtain

$$\boldsymbol{F}_{\text{m}} \equiv \int_A \mathbf{T}_{\text{m}} \mathring{\hat{\boldsymbol{d}}}_3 dX_1 dX_2 = -(\boldsymbol{\mathcal{M}}_0 \cdot \mathring{\hat{\boldsymbol{d}}}_3)\boldsymbol{B}^{\text{a}}, \tag{26}$$

$$\boldsymbol{M}_{\text{m}} \equiv \int_A X_\alpha \hat{\boldsymbol{d}}_\alpha \times (\mathbf{T}_{\text{m}} \mathring{\hat{\boldsymbol{d}}}_3) dX_1 dX_2 = 0. \tag{27}$$

Note that $\boldsymbol{F}_{\text{m}}$ is not necessarily zero, while $\boldsymbol{M}_{\text{m}}$ vanishes for hard-magnetic rods. Similarly to Barreto et al. (2021), $\boldsymbol{F}_{\text{m}}$ does not appear in the magnetic Kirchhoff rod equations (24) and (25), because the *total* internal force $\boldsymbol{F}(s)$ is defined via Eq. (23).

3.4. Reduction of the magnetic Kirchhoff rod equations to planar deformations

In this subsection, for verification purposes, we show that the magnetic Kirchhoff equations derived above can reproduce existing results in the literature for the hard magnetic beams and elastica (Wang et al., 2020; Yan et al., 2021), loaded under a constant or constant gradient magnetic fields. In Wang et al. (2020), a theoretical model under constant field was derived within the continuum framework and validated against experiments. The governing equations for a more general description that can tackle either under constant or constant gradient fields were developed through dimensional reduction and validated experimentally in Yan et al. (2021).

Consider a naturally straight rod clamped at $s = 0$ ($\boldsymbol{r}(0) = \boldsymbol{0}$), while the other end at $s = L$ is set to be force and momentum free. The rod is free from any external forces and torques other than magnetic fields, that is $\boldsymbol{p} = \boldsymbol{q} = 0$. We will derive the governing equation for the bending angle $\theta(s)$ in the x-y plane such that $\theta(s) = 0$ holds in the reference configuration. The constitutive law is $\boldsymbol{M}(s) = EI\theta'(s)\hat{\boldsymbol{e}}_z$. We will study two cases: a naturally straight hard magnetic rod loaded under a constant or constant-gradient fields, which have been studied in Wang et al. (2020) and Yan et al. (2021), respectively.

First, we consider the case of a rod under a *constant* magnetic field $\boldsymbol{B}^{\text{a}} = B^{\text{a}}\hat{\boldsymbol{e}}_y$; see Fig. 2(a). The rod is magnetized as $\boldsymbol{B}^r = -B^r\hat{\boldsymbol{e}}_y$ along the center-line ($\mathring{\hat{\boldsymbol{d}}}_1 = \hat{\boldsymbol{e}}_x$, $\mathring{\hat{\boldsymbol{d}}}_2 = \hat{\boldsymbol{e}}_z$, $\mathring{\hat{\boldsymbol{d}}}_3 = -\hat{\boldsymbol{e}}_y$) with $B^r > 0$ and $B^{\text{a}} > 0$. In the absence of the applied field, the rod is naturally straight along $\hat{\boldsymbol{e}}_y$ as $\mathring{\hat{\boldsymbol{d}}}_3 = -\hat{\boldsymbol{e}}_y$. The Cosserat frame in the reference configuration is given by $\hat{\boldsymbol{d}}_1 = (\cos\theta, \sin\theta, 0)$, $\hat{\boldsymbol{d}}_2 = \hat{\boldsymbol{e}}_z$ and $\hat{\boldsymbol{d}}_3 = (\sin\theta, -\cos\theta, 0)$. Since the applied field is homogeneous, we have $\boldsymbol{p}_{\text{mag}} = 0$ and $\boldsymbol{F}(s) = 0$. To calculate $\boldsymbol{q}_{\text{mag}}$ in Eq. (22), we first need to express $\boldsymbol{\mathcal{M}}$ with respect to θ. From Eq. (9), $\boldsymbol{\mathcal{M}}$ is simplified as

$$\boldsymbol{\mathcal{M}} = \frac{AB^{\text{r}}}{\mu_0}\hat{\boldsymbol{d}}_3. \tag{28}$$

Substituting $\boldsymbol{F}(s) = 0$ and Eq. (28) into the moment balance equation (Eq. (25)), we can reproduce the equation for the hard magnetic elastica (Wang et al., 2020) as

$$EI\theta''(s) + \frac{AB^{\text{r}}B^{\text{a}}}{\mu_0}\sin\theta(s) = 0, \tag{29}$$

with the boundary conditions $\theta(0) = 0$ and $\theta'(L) = 0$. As discussed in Wang et al. (2020), Eq. (29) is mathematically equivalent to the governing equation of the clamped–free elastica. In this configuration, the magnetic rod is known to buckle at the critical applied field (Wang et al., 2020)

$$B^{\text{a}*}_{\text{bend}} = \left(\frac{\pi}{2}\right)^2 \frac{\mu_0 EI}{AB^r L^2}, \tag{30}$$

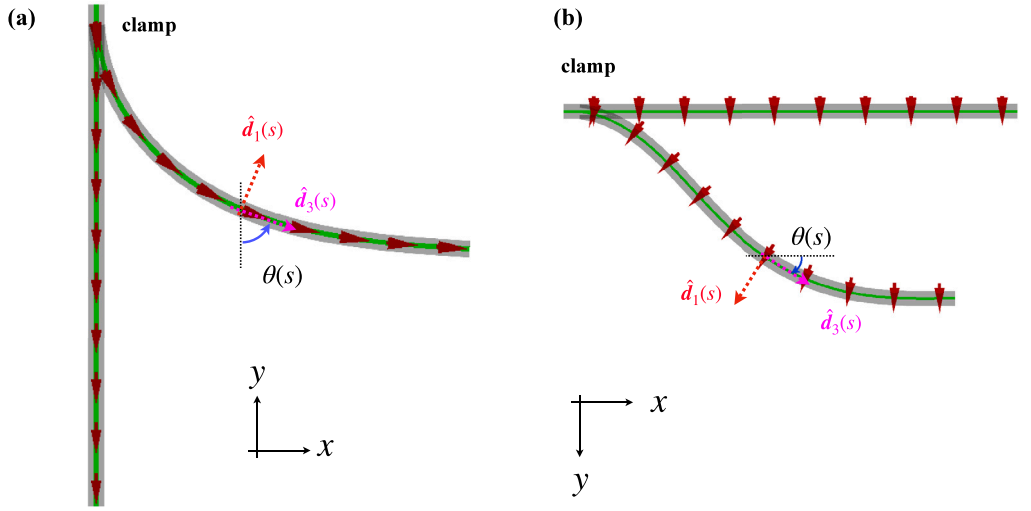

Fig. 2. Reduction of magnetic Kirchhoff rod equations to planar cases. (a) Schematics of a hard magnetic rod under constant field that deforms in two dimensions. The rod is magnetized along the tangent of the rod centerline $\hat{\boldsymbol{d}}_3$. (b) Schematics of a hard magnetic rod under constant *gradient* field. The rod is magnetized along $\hat{\boldsymbol{d}}_1$.

a result that will be used in Section 6.2 to connect our three-dimensional analytical results with the existing two-dimensional results in literature (Wang et al., 2020).

Second, we consider the case of a rod in a *constant gradient* magnetic field: $\boldsymbol{B}^{\mathrm{a}}(\boldsymbol{r}) = by\hat{\boldsymbol{e}}_y$, where b is a constant. The rod is clamped along $\hat{\boldsymbol{e}}_x$ ($y = 0$) and magnetized as $\boldsymbol{B}^{\mathrm{r}} = B^{\mathrm{r}}\hat{\boldsymbol{e}}_y$ (Fig. 2(b)). The Cosserat frame in the reference configuration is given by $\mathring{\hat{\boldsymbol{d}}}_1 = \hat{\boldsymbol{e}}_y$, $\mathring{\hat{\boldsymbol{d}}}_2 = \hat{\boldsymbol{e}}_z$, and $\mathring{\hat{\boldsymbol{d}}}_3 = \hat{\boldsymbol{e}}_x$. We can write the Cosserat frame in the deformed configuration as $\hat{\boldsymbol{d}}_1 = -\sin\theta\hat{\boldsymbol{e}}_x + \cos\theta\hat{\boldsymbol{e}}_y$, $\hat{\boldsymbol{d}}_2 = \hat{\boldsymbol{e}}_z$, and $\hat{\boldsymbol{d}}_3 = \cos\theta\hat{\boldsymbol{e}}_x + \sin\theta\hat{\boldsymbol{e}}_y$. Hence, the magnetization vector is simplified from Eq. (9) as

$$\boldsymbol{\mathcal{M}} = \frac{AB^{\mathrm{r}}}{\mu_0}\hat{\boldsymbol{d}}_1. \tag{31}$$

Given that the rod is in a constant gradient field, $\boldsymbol{p}_{\mathrm{mag}}$ is non-zero. From Eqs. (21) and (31), we find $\boldsymbol{p}_{\mathrm{mag}}(s) = (AB^{\mathrm{r}}b/\mu_0)\cos\theta(s)\,\hat{\boldsymbol{e}}_y$. The force balance in Eq. (24) can now be integrated as

$$\begin{aligned}\boldsymbol{F}(s) &= \boldsymbol{F}(L) + \int_s^L \boldsymbol{p}_{\mathrm{mag}}(s')ds' \\ &= \frac{AB^{r}b}{\mu_0}\hat{\boldsymbol{e}}_y\int_s^L \cos\theta(s')ds'.\end{aligned} \tag{32}$$

Plugging this result into the moment balance in Eq. (25), we obtain the following integro-differential equation

$$EI\frac{d^2\theta}{ds^2} - \frac{AB^{r}b}{\mu_0}\left\{y(s)\sin\theta(s) - \cos\theta(s)\int_s^1 \cos\theta(s')ds'\right\} = 0, \tag{33}$$

whose second and third terms originate from distributed magnetic torque and force, respectively. Eq. (33) has been recently derived and validated experimentally in Wang et al. (2020), Yan et al. (2021), verifying our reduced framework presented in this section.

We note that the inhomogeneous applied field can be interpreted as a distributed load on the magnetic rod. Indeed, in the limit of small bending angle $\theta \ll 1$, Eq. (33) is identical to that of an elastica under gravity (Wang, 1986). By analogy with the gravitational case, we can introduce the *magneto-bending* length ℓ_m as

$$\ell_m \equiv \left(\frac{\mu_0 EI}{AB^{\mathrm{r}}b}\right)^{1/3}, \tag{34}$$

which can be regarded as a (persistence) length quantifying the relative importance of the magnetic and elastic effects. When $\lambda_m \equiv L/\ell_m \ll 1$, the gradient of the magnetic field is negligible, while in the case of $\lambda_m \gg 1$, the magnetic gradient plays an important role in the bending of the magnetic rod.

We have shown that the magnetic Kirchhoff rod equations derived in Section 3.3 are able to reproduce existing results reported in Wang et al. (2020), Yan et al. (2021) for the planar deformation of the magnetic rod. The specialization to the two-dimensional cases verifies our theory, even if only partially. In the following sections, we will combine discrete simulation and precision experiments to study non-planar (three-dimensional) deformations of the rod, toward the validation of our theoretical framework.

4. Discrete simulations of magneto-elastic rods

Although our magnetic Kirchhoff rod model reproduces the governing equation of planar hard magnetic beams and elastica, computing the nonlinear geometric deformation in three dimensions requires, in general, a numerical approach. Specifically, we discretize the rod-centerline as a set of connected particles via straight segments (Chirico and Langowski, 1994; Wada and Netz, 2007b,a; Vogel and Stark, 2010; Reichert, 2006; Bergou et al., 2008; Morigaki et al., 2016; Sano et al., 2017; Sano and Wada, 2018, 2019). This discrete method is widely used to simulate the large deformation of rod-like structures such as nano-springs (Wada and Netz, 2007b), DNA (Chirico and Langowski, 1994), helical bacteria (Wada and Netz, 2007a), flagella (Reichert, 2006; Vogel and Stark, 2010), human hairs (Bergou et al., 2008), and gift-wrapping ribbons (Morigaki et al., 2016; Sano et al., 2017; Sano and Wada, 2018, 2019). Within this computational framework, the rod centerline is regarded as the chain of straight segments of natural length ℓ_0 and an equal mass $m = \rho AL/N$. At each node $i = 1, 2, \dots, N$, we assigned a discrete Cosserat frame basis vectors $(\hat{\boldsymbol{d}}_{1,i}, \hat{\boldsymbol{d}}_{2,i}, \hat{\boldsymbol{d}}_{3,i})$, corresponding to $\hat{\boldsymbol{d}}_a$ in the continuum model. The elastic bending and twist deformations are represented by the Euler angles between adjacent discretized Cosserat frame basis vectors (Chirico and Langowski, 1994; Wada and Netz, 2007b,a; Reichert, 2006; Vogel and Stark, 2010; Bergou et al., 2008; Morigaki et al., 2016; Sano et al., 2017; Sano and Wada, 2018, 2019).

In the present section, we detail the simulation method, with a particular focus on the discrete versions for the distributed magneto-elastic forces, $\mathcal{P}$, and torques, $\mathcal{Q}$, in Section 4.1. The equations of motion for the discrete segments follow in Section 4.2. We summarize the derivation of the elastic bending and twisting forces and torques in Appendix A.

4.1. Magneto-elastic force and torque in the discrete simulation

To compute the nonlinear geometric deformation of our rod-like magnetic structures, we adopt dynamic simulations, instead of solving the static equilibrium equations. Static analysis packages for ODEs (*e.g.*, AUTO (Doedel, 1981)) would have enabled path following and the analysis of the bifurcation diagram for all stable and unstable branches. However, the purpose of our simulation is to reproduce the stable configuration observed experimentally so as to serve in the validation of our theoretical model for magnetic rods. To facilitate numerical convergence to the mechanical equilibrium, we perform the dynamic simulation by including the inertial terms in Eqs. (24) and (25). Specifically, we will derive the elastic and magneto-elastic loads from the variation of $E_{\rm el}$ and $E_{\rm mag}$ with respect to the set of $(\delta \boldsymbol{r}, \delta\chi_3)$. We recall that the expressions of the distributed magneto-elastic force $\boldsymbol{p}_{\rm mag}$ and torque $\boldsymbol{q}_{\rm mag}$, provided in Eqs. (20)–(22), have been derived from the continuum framework, through the variation $\delta E_{\rm mag}$ with respect to the set of $(\delta \boldsymbol{r}, \boldsymbol{\epsilon})$. The set of infinitesimal bending and twist angles were represented by $\boldsymbol{\epsilon} = \delta\chi_a \hat{\boldsymbol{d}}_a$ as in Section 3.2. In the discrete simulation framework (Chirico and Langowski, 1994; Wada and Netz, 2007b,a; Vogel and Stark, 2010; Reichert, 2006; Bergou et al., 2008; Morigaki et al., 2016; Sano et al., 2017; Sano and Wada, 2018, 2019), the elastic forces and axial torques, which are calculated from the set of $(\delta \boldsymbol{r}, \delta\chi_3)$, are used to compute the set of velocities and angular velocities around $\hat{\boldsymbol{d}}_{3,i}$ of the node $(\boldsymbol{v}_i, \omega_{3,i})$. Based on $(\boldsymbol{v}_i, \omega_{3,i})$, the position of the node $\boldsymbol{r}_i$ and the *angular parameter* φ_i are constructed as

$$\boldsymbol{r}_i(t) \equiv \int_0^t \boldsymbol{v}_i(t')dt', \tag{35}$$

$$\varphi_i(t) \equiv \int_0^t \omega_{3,i}(t')dt'. \tag{36}$$

Note that although the infinitesimal angle $\delta\chi_3$ is well-defined, there is no globally defined single function $\chi_3(s,t)$ whose spatial and time derivative gives the correct Ω_3 and ω, respectively. In other words, $\chi_3(s,t)$ is not a single function that specify the rod configuration, because pure bending of a curved rod can vary its twist (see, for example, Goldstein et al. (1998)). It is only the variation $\delta\chi_3$, defined as $\delta\chi_3 \equiv (\delta\hat{\boldsymbol{d}}_1)\cdot\hat{\boldsymbol{d}}_2 = -(\delta\hat{\boldsymbol{d}}_2)\cdot\hat{\boldsymbol{d}}_1$, that is meaningful and used to calculate the numerical elastic force and torque (Powers, 2010). (The remaining infinitesimal bending angles $\delta\chi_1 = -(\delta\boldsymbol{r})'\cdot\hat{\boldsymbol{d}}_2$, $\delta\chi_2 = (\delta\boldsymbol{r})'\cdot\hat{\boldsymbol{d}}_1$ are unnecessary in the simulations.) More details on this point are provided in Appendix A. Nevertheless, through the time-series data of ω_i, we can *define* the virtual angular parameter φ_i, as Eq. (36). The resulting φ_i obtained from Eq. (36) is not a single-valued function, which depends on the history of how the rod centerline is evolved. However, the specific value of φ_i is inconsequential to the simulation of the deformation of the rod-configuration. Indeed, the simulation outputs the correct centerline position $\boldsymbol{r}$ and twist density Ω_3, irrespective of the value of φ_i computed in the background; only $\delta\chi_{3,i}$ appears explicitly in the computation of the elastic forces and torques and not φ_i (see Appendix A). The similar solution strategy has been employed previously in the literature (Chirico and Langowski, 1994; Wada and Netz, 2007b,a; Vogel and Stark, 2010; Reichert, 2006; Bergou et al., 2008; Morigaki et al., 2016; Sano et al., 2017; Sano and Wada, 2018, 2019). To include the distributed magneto-elastic force and torque in the equations of motion based on $(\delta \boldsymbol{r}, \delta\chi_3)$, we will introduce the discrete version of $(\boldsymbol{p}_{\rm mag}, \boldsymbol{q}_{\rm mag})$, as $(\mathcal{P}, \mathcal{Q})$, by rewriting $\delta E_{\rm mag}$ (Eq. (20)) with respect to the set of $(\delta \boldsymbol{r}, \delta\chi_3)$. The discrete version of the magneto-elastic torque $\mathcal{Q}$ (a scalar) will correspond to the magneto-elastic torque around $\hat{\boldsymbol{d}}_3$, while the remaining components of $\boldsymbol{q}_{\rm mag}$ (*i.e.*, $q_{\rm mag1}$ and $q_{\rm mag2}$) will be included in the equation of motion for $\boldsymbol{r}$, thereby defining $\mathcal{P}$, as we detail below.

Expressing $\delta\chi_1$ and $\delta\chi_2$ from Eq. (20) with the aid of $\delta\chi_1 = -(\delta\boldsymbol{r})'\cdot\hat{\boldsymbol{d}}_2$ and $\delta\chi_2 = (\delta\boldsymbol{r})'\cdot\hat{\boldsymbol{d}}_1$, we find the following equation after the partial integration of $(\delta\boldsymbol{r})'$:

$$\begin{aligned}\delta E_{\rm mag} &= -\int_0^L [\delta\boldsymbol{r}(s)\cdot\boldsymbol{p}_{\rm mag}(s) + \boldsymbol{\epsilon}(s)\cdot\boldsymbol{q}_{\rm mag}(s)]ds \\ &= -\int_0^L [\delta\boldsymbol{r}\cdot\boldsymbol{p}_{\rm mag} + \delta\chi_1 q_{\rm mag1} + \delta\chi_2 q_{\rm mag2} + \delta\chi_3 q_{\rm mag3}]ds\end{aligned}$$

$$= -\int_0^L [\delta \boldsymbol{r} \cdot \boldsymbol{p}_{\rm mag} + \{-(\delta \boldsymbol{r})' \cdot \hat{\boldsymbol{d}}_2\} q_{\rm mag1} + \{(\delta \boldsymbol{r})' \cdot \hat{\boldsymbol{d}}_1\} q_{\rm mag2} + \delta\chi_3 q_{\rm mag3}] ds$$

$$= -\int_0^L \left[\delta \boldsymbol{r} \cdot \boldsymbol{\mathcal{P}} + \delta\chi_3 \mathcal{Q}\right] ds + \left[\delta \boldsymbol{r} \cdot \left\{q_{\rm mag1} \hat{\boldsymbol{d}}_2 - q_{\rm mag2} \hat{\boldsymbol{d}}_1\right\}\right]_0^L, \tag{37}$$

where we introduce the $a(=1,2,3)$th component of the magnetic torque $q_{{\rm mag}a} = \boldsymbol{q}_{\rm mag} \cdot \hat{\boldsymbol{d}}_a$. Here, we define the discrete version of the distributed elasto magnetic force and torque as

$$\boldsymbol{\mathcal{P}} \equiv \boldsymbol{p}_{\rm mag} + \left(q_{\rm mag1} \hat{\boldsymbol{d}}_2 - q_{\rm mag2} \hat{\boldsymbol{d}}_1\right)', \tag{38}$$

$$\mathcal{Q} \equiv q_{\rm mag3}\,, \tag{39}$$

which will be used to formulate the discrete version of the equations of motion. Note that $q_{\rm mag1}$ and $q_{\rm mag2}$ are now included in $\boldsymbol{\mathcal{P}}$, appropriately. In the next subsection, we incorporate the magneto-elastic force and torque through $\boldsymbol{\mathcal{P}}$ and $\mathcal{Q}$ into the equations of motion for the centerline velocity and the angular velocity $(\boldsymbol{v}, \omega_3)$.

4.2. Equations of motion used in the discrete simulations

In this subsection, we derive the discrete version of the equation of motion for the MRE rod by adding $(\boldsymbol{\mathcal{P}}, \mathcal{Q})$ into the equation of motion for the centerline velocity and the angular velocity $(\boldsymbol{v}, \omega_3)$. We start from the magnetic Kirchhoff equations that we derived earlier, with the sole addition of the inertial terms

$$\rho A \frac{\partial \boldsymbol{v}}{\partial t} = \frac{\partial \boldsymbol{F}}{\partial s} + \boldsymbol{p} + \boldsymbol{\mathcal{P}}, \tag{40}$$

$$\frac{\partial \boldsymbol{L}}{\partial t} = \frac{\partial \boldsymbol{M}}{\partial s} + \hat{\boldsymbol{d}}_3 \times \boldsymbol{F} + \boldsymbol{q} + \mathcal{Q}\hat{\boldsymbol{d}}_3, \tag{41}$$

where $(\boldsymbol{p}_{\rm mag}, \boldsymbol{q}_{\rm mag})$ are replaced by $(\boldsymbol{\mathcal{P}}, \mathcal{Q}\hat{\boldsymbol{d}}_3)$, as derived in the previous section. The left hand sides of Eq. (41) represent the inertia terms. Here, we define the velocity of the centerline $\boldsymbol{v}(s,t) = \partial \boldsymbol{r}/\partial t$, the angular momentum per unit length $\boldsymbol{L} = I_a \omega_a \hat{\boldsymbol{d}}_a$, and the angular velocity vector $\boldsymbol{\omega}(s,t) = \omega_a \hat{\boldsymbol{d}}_a$, with the mass density per unit volume ρ and the principal moments of inertia of the cross section $I_1 = I_2 = I$ and $I_3 = I_1 + I_2 = 2I$ (Goldstein et al., 2002). The angular velocity vector $\boldsymbol{\omega}$ describes the rotation rates of $\hat{\boldsymbol{d}}_a$ in time as

$$\frac{\partial \hat{\boldsymbol{d}}_a}{\partial t} = \boldsymbol{\omega} \times \hat{\boldsymbol{d}}_a\,. \tag{42}$$

To ensure that the rod relaxes to the mechanical equilibrium, we include *numerical* drag forces and torque acting on the rod-centerline per unit length through $\boldsymbol{p} = -\gamma_t \boldsymbol{v}$ and $\boldsymbol{q} = -\gamma_r \omega_3 \hat{\boldsymbol{d}}_3$. We readily derive the dynamic equations of twist around $\hat{\boldsymbol{d}}_3$ by taking the inner product between the moment balance equation and $\hat{\boldsymbol{d}}_3$. Then, introducing the internal elastic forces $\boldsymbol{f}$ and the axial torque T per unit length as

$$\boldsymbol{f} \equiv \frac{\partial \boldsymbol{F}}{\partial s}, \quad T \equiv \frac{\partial M_3}{\partial s} + M_2 \Omega_1 - M_1 \Omega_2, \tag{43}$$

we rewrite Eqs. (40) and (41) as

$$\rho A \frac{\partial \boldsymbol{v}}{\partial t} = \boldsymbol{f} + \boldsymbol{p} + \boldsymbol{\mathcal{P}}, \tag{44}$$

$$I_3 \frac{\partial \omega_3}{\partial t} = T - \gamma_r \omega_3 + \mathcal{Q}, \tag{45}$$

respectively. We solve Eqs. (44) and (45) for the discrete versions of the centerline velocity and the angular velocity $(\boldsymbol{v}, \boldsymbol{\omega}_3)$. Choosing the units of mass, length, and force as $m\ell_0$, ℓ_0 and EI/ℓ_0^2, respectively, we non-dimensionalize Eqs. (44) and (45) as

$$\frac{\partial \tilde{\boldsymbol{v}}_i}{\partial t} = \tilde{\boldsymbol{f}}_i + \tilde{\boldsymbol{p}}_i + \tilde{\boldsymbol{\mathcal{P}}}_i, \tag{46}$$

$$\tilde{I}_3 \frac{\partial \tilde{\omega}_{3,i}}{\partial t} = \tilde{T}_i - \tilde{\gamma}_r \tilde{\omega}_{3,i} + \tilde{\mathcal{Q}}_i, \tag{47}$$

where quantities with $\tilde{(\cdot)}$ represent the corresponding dimensionless variables.

The numerical scheme for calculating the elastic force $\boldsymbol{f}_i$ and axial torque T_i at each node i follows that of Chirico and Langowski (1994), Wada and Netz (2007b,a), Vogel and Stark (2010), Reichert (2006), which are briefly summarized in Appendix A. In short, we employ the Euler angle representation to describe the configuration of the discrete director frames at each point. The Darboux vector components in the discretized model, $\Omega_{a,i}$ $(a = 1,2,3)$, and the corresponding discretized elastic energy can be expressed in terms of the three Euler angles. The variation of the elastic energy $E_{\rm el}$ is related to $(\delta \boldsymbol{r}, \delta\chi_3)$ through the variations of the corresponding Euler angles, from which we find the bending and twisting forces acting on each node of the chain (Chirico and Langowski, 1994; Wada and Netz, 2007b,a; Vogel and Stark, 2010; Reichert, 2006). All values of the dimensionless parameters are taken from the experiments, which will be presented in Section 5, such that our simulations do not contain any free parameters. We performed the simulation for a sufficiently long time such that the rod relaxes to the mechanical equilibrium (typically $10^7 - 10^9$ discrete time steps), where the number of nodes lies within the range $40 \le N \le 120$. We use the two-step Adams–Bashforth method (Hairer et al., 1993) to numerically integrate the re-scaled dynamical equations in Eq. (47) with non-dimensional time steps, typically ranging between 10^{-3}–10^{-1}, to ensure sufficient numerical accuracy. The director frames at each node are also updated at each time step, and the corresponding Euler angles are calculated for a new configuration.

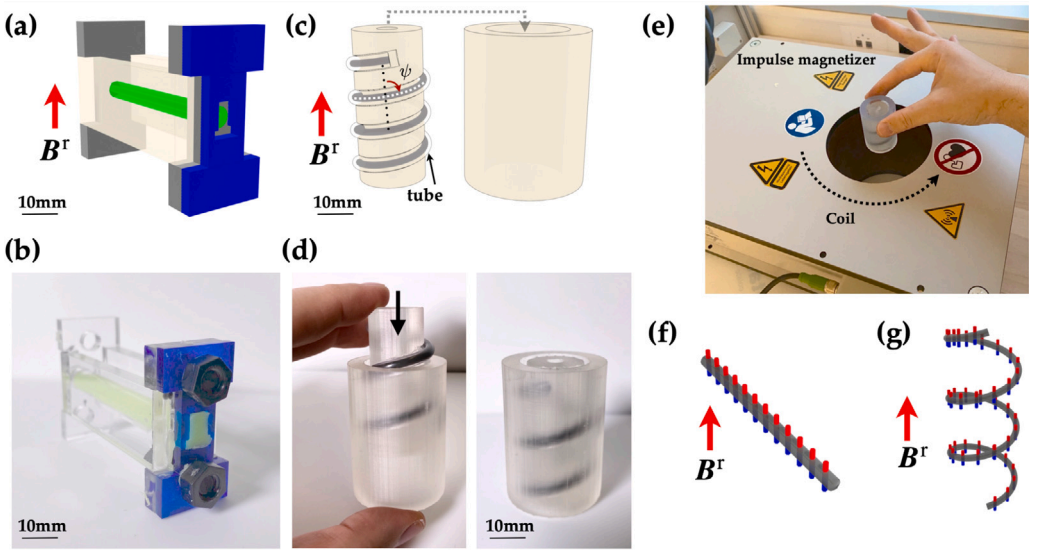

Fig. 3. Fabrication procedure to manufacture straight and helical rods made out of a MRE. (a) Schematic diagram of the mold for a straight rod. A straight acrylic tube (green) is threaded into two parallel supporting plates. (b) Photograph of the mold used to produce a straight rod. (c) Schematic diagram of the mold for a helical rod. A rigid cylinder with a helical groove (inner mold) is 3D printed. (d) Photograph of the mold for a helical rods. (e) The mold with the cured elastomer is placed into an impulse magnetizer such that $\boldsymbol{B}^r$ in (a) and (c) is aligned with the axis of the coil. Schematics of a magnetized (f) straight and (g) helical rod. The local magnetization vectors are depicted by the embedded "magnets", where the red and blue ends correspond to the north and south poles, respectively.

5. Experimental fabrication, apparatus, and protocols

We perform three different sets of experiments to validate our theory presented in Section 3: (i) a naturally straight rod under a constant field, (ii) a helical rod under a constant field, and (iii) a helical rod under a constant gradient field. We chose these three configurations because previous works (Wang, 1986; Ciambella and Tomassetti, 2020; Wang et al., 2020; Yan et al., 2021) were limited to the case of straight beams, without twist deformations. For case (i), we still consider a straight rod but also include twist deformation. Through case (ii), we can individually validate the magneto-elastic torque $\boldsymbol{q}_{\text{mag}}$. In case (iii), both $\boldsymbol{q}_{\text{mag}}$ and $\boldsymbol{p}_{\text{mag}}$ can be validated. In this section, we present the details of our experiments, whose results will be provided in Section 6. To perform the experiments, in Section 5.1, we detail the procedure that we developed to manufacture our MRE rods. In Section 5.2, we present the design of the magnetic coils used to generate the magnetic field. The detailed protocols for the cases (i)–(iii) follow in Section 5.3.

5.1. Fabrication of hard magnetic rods

Our rods were made of a magnetorheological elastomer (MRE), a composite of hard-magnetic NdPrFeB particles and vinylpolysiloxane (VPS) polymer (Young's modulus $E_{\text{vps}} = 1.16 \pm 0.03$ MPa, Poisson's ratio $\nu = 0.5$ and mass density $\rho_{\text{vps}} = 1.17 \pm 0.26$ g/cm^3). The fabrication of the MRE rods involved the following steps. First, the non-magnetized NdPrFeB particles (average size of 5 μm, mass density $\rho_{\text{mag}} = 7.61$ g/cm^3 MQFP-15-7-20065-089, Magnequench) of weight m_{mag} were mixed with the VPS base liquid solution (Elite Double 32, Zhermack) of weight m_{base} using a centrifugal mixer (ARE-250, Thinky Corporation). Secondly, the VPS catalyst (weight $m_{\text{cat}} = m_{\text{base}}$) was added to the mixed solution with a ratio of 1:1 in weight to the VPS base. The solution of total weight $m_{\text{tot}} = m_{\text{mag}} + m_{\text{base}} + m_{\text{cat}}$ was then mixed using the centrifugal mixer for 40 s at 2000 rpm (clockwise), and another 20 s at 2200 rpm (counterclockwise). We further degassed the solution in a vacuum chamber (absolute pressure below 8 mbar) to remove any air bubbles that could otherwise compromise the homogeneity of the MRE. The final solution was injected into the molds (detailed in the next paragraph) using a syringe to cast either straight or helical rods. We varied the mass concentration ratio for NdPrFeB particles in the range $c = m_{\text{mag}}/m_{\text{tot}} = 10 - 30\%$.

The schematic and a photograph of a mold used to fabricate a straight rod are shown in Fig. 3(a) and (b), respectively. We injected the mixed solution into a straight acrylic tube (Plexiglas XT tubes incolore 0A070, Röhm, Switzerland, inner diameter 2 or 4 mm) threaded into two coaxial holes in acrylic plates. One of the inlets of the tube was designed to have a convex shape pointing to the direction of the residual flux density. The convex inlet is utilized to align the magnetization vector $\boldsymbol{B}^r$ precisely.

To fabricate helical rods, we prepared a rigid cylinder of diameter 20 mm with a helical half-piped groove (diameter 4.5 mm) using a 3D printer (Printer: Form 2, Formlabs, Material: Clear Resin (RS-F2-GPCL-04)). The schematic and the photograph of the mold with a helical groove are shown in Fig. 3(c) and (d), respectively. A flexible tube (diameter 4 mm, Misumi) is placed along the groove, injecting the mixed solution into it. The inner mold and the tube were then positioned inside a 3D printed (outer) cylinder (inner diameter 12 mm and outer diameter 16 mm). The central axis of the helical groove and that of the outer cylinder were set

co-axially. The 3D printed molds allowed us to control the pitch angle ψ of a helical MRE rod up to $\psi \lesssim 1.49$ rad. For larger values of ψ, we prepared the acrylic cylinder (without a groove) and tightly spooled a flexible tube around it with a pitch angle of $\psi = 1.51$ rad.

After injection of the mixed solution into either the straight or helical molds, the curing of the polymer mixture occurred in approximately 20 min, at room temperature. The (projected) radius of the helical centerline was chosen to be $R = 10$ mm to minimize the deformation of the tube, allowing us to have a cross-section of the helix close to circular, which could otherwise deviate from the circular shape for tighter helices due to the Brazier instability (Brazier, 1927).

Before demolding, the rods were magnetized permanently by saturating the NdPrFeB particles in the MRE using an applied uniaxial magnetic field (4.4 or 2.5 T) generated by an impulse magnetizer (IM-K-010020-A Magnet-Physik Dr. Steingroever GmbH), as shown in Fig. 3(e). The directions of $\boldsymbol{B}^{\mathrm{r}}$ for either a straight or helical rods were set normal to the cross section or parallel to the central axis of a helix, respectively. Schematic diagrams for the magnetized straight and helical rods are shown in Figs. 3 (f) and (g), respectively. The fabricated MRE rods possessed the residual flux densities of $|\boldsymbol{B}^{\mathrm{r}}| = 0.90 c_v$ T (Sections 6.1 and 6.3) and $|\boldsymbol{B}^{\mathrm{r}}| = 0.86 c_v$ T (Section 6.2). The Young's modulus was $E = E_{\mathrm{vps}}/(1 - c_v^{1/2})$ with the volume concentration of the particles equal to $c_v = (1 + (\rho_{\mathrm{mag}}/\rho_{vps})(m_{\mathrm{tot}}/m_{\mathrm{mag}} - 1))^{-1}$ (Counto, 1964). After magnetization, the rods were demolded and cut to the desired length L (within an experimental uncertainty of ± 1 mm).

5.2. Experimental apparatus

During the experimental tests, the samples are loaded magnetically by placing them in between a set of two coaxial coils, which induce a steady axial symmetric magnetic flux $\boldsymbol{B}^{\mathrm{a}}(r, z)$ (Yan et al., 2021). Each coil is manufactured by winding an aluminum circular spool with an insulated magnet wire (Repelec Moteurs S.A.). The magnet wire (enameled wire, Isomet AG) has a circular cross-section of diameter 1.32 mm for the copper core and thickness 0.102 mm for the outer insulation layer. The final dimensions of the coil are 86 mm in inner diameter, 152 mm in outer diameter, and 43 mm (33 mm for wires and 10 mm for the spool) in height; the mean radius of the coil $\mathcal{R}$ is $\mathcal{R} = 59.5$ mm. The coils are powered by a DC power supply providing a maximum current to power ratio of 25 A/1.5 kW (EA-PSI 9200-25T, EA-Elektro-Automatik GmbH).

The two identical coils are set co-axially along $\hat{e}_z$ and their current can flow in either the same or opposite directions. To realize a *constant (homogeneous) field*, the center-to-center axial distance is set to be 59.5 mm($= \mathcal{R}$), and the current in the coils is set to flow in the same direction; this is known as the Helmholtz coil configuration. In the central region between the coils, the field generated by the Helmholtz coil is

$$\boldsymbol{B}^{\mathrm{a}} = B^{\mathrm{a}} \hat{e}_z. \tag{48}$$

In contrast, to realize the *constant gradient field*, the center-to-center axial distance is set to be 103 mm ($= \sqrt{3}\mathcal{R}$), and the current in the coils is set to flow in opposite directions. This configuration is known as the Maxwell coil, where the magnetic field induced near the coil is

$$\boldsymbol{B}^{\mathrm{a}}(r, z) = -\frac{b}{2} r \hat{\boldsymbol{e}}_r + b z \hat{\boldsymbol{e}}_z. \tag{49}$$

In this Maxwell coil configuration, the gradient of the magnetic field is $b = (\partial_z \boldsymbol{B}^{\mathrm{a}}) \cdot \hat{\boldsymbol{e}}_z$, i.e. constant. From the Gauss law of magnetism, $\nabla \cdot \boldsymbol{B}^{\mathrm{a}} = 0$, there are gradient components in both the radial, $\hat{\boldsymbol{e}}_r$, and the $\hat{\boldsymbol{e}}_z$ directions.

We characterized the relationship between the flux density and the current in the coils, I_c, by using a Teslameter (FH 55, Magnet-Physik Dr. Steingroever GmbH) and the results are plotted in Fig. 4. The fields described by Eqs. (48) and (49) are realized in the region of $z, r \lesssim 0.6\mathcal{R}$. For the Helmholtz configuration, the constant field is induced near the center, for several values of I_c. In Fig. 4(a), we plot the profiles of the measured field $\boldsymbol{B}^{\mathrm{a}}$ divided by I_c, which collapse onto a single curve. This collapse confirms that, $\boldsymbol{B}^{\mathrm{a}}$ is proportional to I_a. By fitting the constant B^{a} near the center, we find $\boldsymbol{B}^{\mathrm{a}}$ and I_a as $B_a/I_c = 8.9$ mT/A. For the Maxwell configuration, a constant gradient field is generated near the center of the coils (Fig. 4(b) and (c)). We measured the profiles of the induced field both along with $\hat{\boldsymbol{e}}_z$ and $\hat{\boldsymbol{e}}_r$ for different values of I_c. The data again collapse on a single curve as $\boldsymbol{B}^{\mathrm{a}}/I_c$, which implies that the gradient of the field b is linearly proportional to I_c. By fitting the field along $\hat{\boldsymbol{e}}_z$, we find $b/I_c = 0.133$ T/(A m). From Eq. (49), the gradient along $\hat{\boldsymbol{e}}_r$ is half of that along $\hat{\boldsymbol{e}}_z$. In Fig. 4(c), we plot the slope of $b/2$ as the dashed line, which is in an excellent agreement with the measurement. This experimental characterization confirms that our coils accurately produce the fields according to Eqs. (48) and (49) when set in either the Helmholtz or the Maxwell configurations, respectively.

5.3. Experimental protocols

Having described the experimental apparatus above, we proceed by presenting the protocols that we followed during the experiments. We placed the samples (prepared through the procedure detailed in Section 5.1) between the coils (whose field was characterized in the previous section). First, we will study the deformation of a straight or curved rod under the constant field (Helmholtz coil) followed by the study of the deformation of a helix under the constant gradient field (Maxwell coil), as shown in Fig. 5(a)–(d). A photograph of our apparatus is shown in Fig. 5(a). All the experimental results for the corresponding setups will be presented in Section 6. The protocols for each experiment are detailed next.

In Section 6.1, we will present results on the deformation of a straight rod under constant field. For these experiments, our MRE rods were magnetized along $-\hat{\boldsymbol{e}}_z$, and a constant magnetic field was applied along $\hat{\boldsymbol{e}}_z$; see Fig. 5(b). An acrylic clamp, engraved to have the convex shape at one of the ends of the rod, hanged the rod from above. This clamp was also designed such that

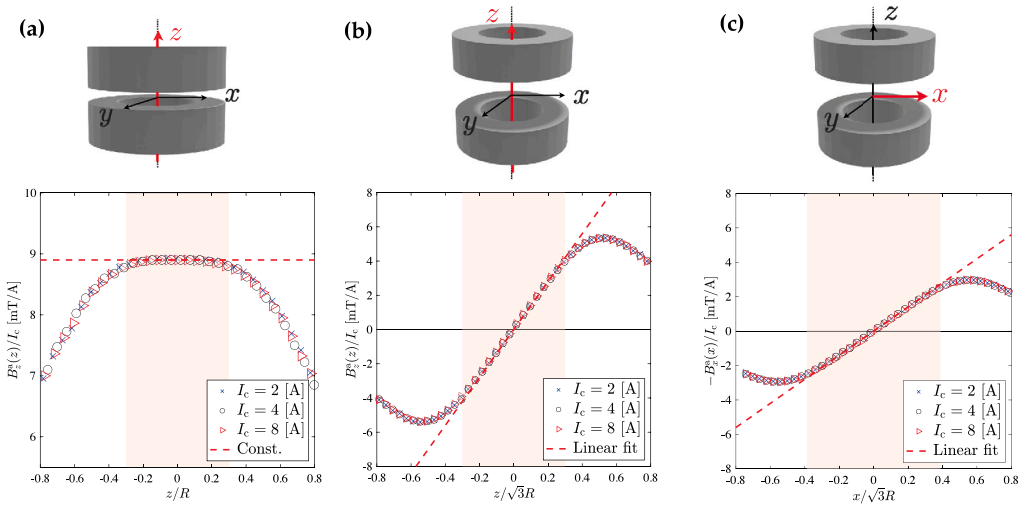

Fig. 4. Experimental characterization of the field generated by the magnetic coils in the (a) Helmholtz (constant field) and (b, c) Maxwell (constant gradient field) configurations. (a) Profile of the (rescaled) applied field along $x = y = 0$. Profile of the applied field along (b) $x = y = 0$ and (c) $y = z = 0$. The dashed lines in the plot correspond to the (a) constant and (b) (c) linear fits within the shaded regions where the experiments were performed.

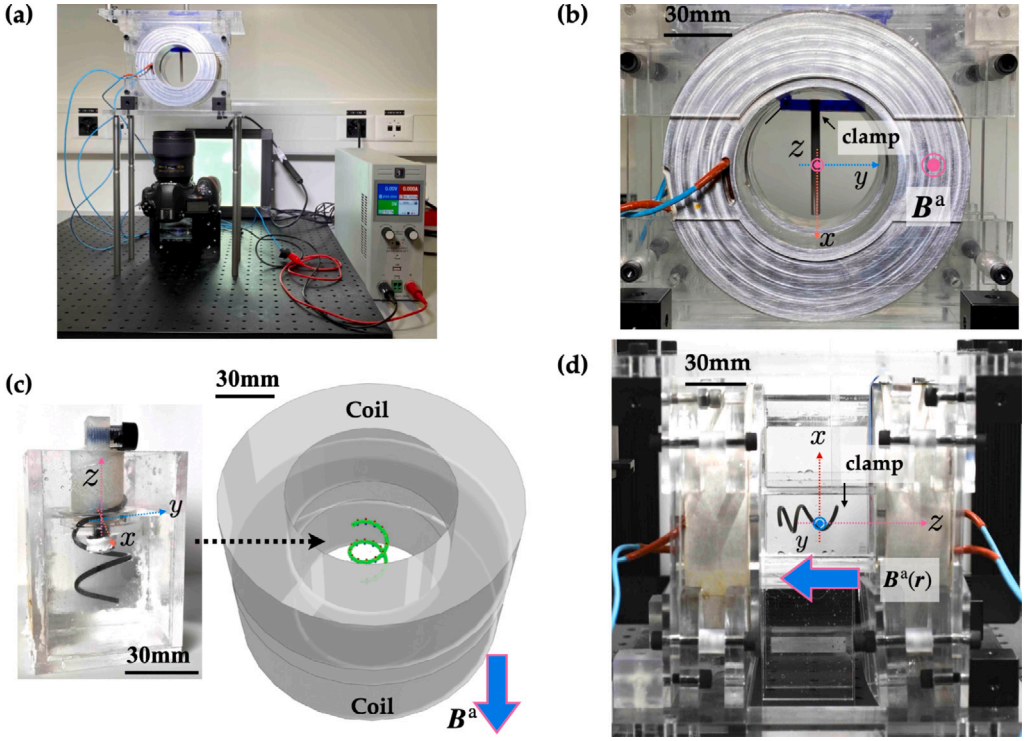

Fig. 5. (a) Photograph of the full experimental apparatus. A single power supply generates the electric current provided to the two coils. A digital camera set underneath the coils captures the deformation of the rod. (b) Experimental setup used for the twist instability of a straight rod (Section 6.1). The straight rod magnetized along $-\hat{e}_z$ is clamped along $\hat{e}_x$. The applied field $\boldsymbol{B}^a$ is set as shown in Eq. (48). (c) The schematic of the experimental setup for a helix under constant field (right panel, See Section 6.2), with the uniformly helical magnetic rod (left panel). The helix magnetized along $\hat{e}_z$ is clamped such that its central axis is parallel to that of the coils. The magnetic helix is immersed in a glycerol bath. (d) Photograph of a magnetic helical rod (in the glycerol bath) under constant gradient field (Section 6.3).

its width matched the gap between the coils (13.5 mm). We varied the total length of the rod in the ranges $L = 40$–57 mm, the mass concentration ratio of NdPrFeB particles is $c = 10,\ 20,\ 30\%$, and the rod diameter was $d = 3,5$ mm. We measured the twist

deformation of the rod (detailed in the next section) using a digital camera, placed underneath the setup and directed upwards. The measured twisting angles were averaged over 4 or 5 samples.

In Section 6.2, we will study the deformation of a helical rod under the constant field. For these experiments, the helix was clamped vertically by a 3D-printed rigid cylinder such that its central axis was parallel to the coil axis ($\hat{\boldsymbol{e}}_z$). The constant magnetic field (Eq. (48)) was applied (anti-parallel to $\boldsymbol{B}^{\mathrm{r}}$) to the helical rod magnetized along $\hat{\boldsymbol{e}}_z$, as shown in Fig. 5(c). The experiments were performed in a glycerol bath (85%, 1.23 g/cm^3, Sigma-Aldrich), which density-matched the rods, thereby minimizing the effect of gravity. We performed experiments for the MRE rod of diameter 2 mm, pitch angle $\psi = 1.28$ rad, and radius of curvature $R = 10$ mm. The total length L and the concentration ratio c were varied in the ranges $L = 40$–120 mm and $c = 10, 20\%$, respectively.

For the results in Sections 6.3 and 7, we applied a constant gradient field (according to Eq. (49)) to a helical rod, whose central axis in the reference configuration was chosen to be aligned with the axis of the coils (z-axis, perpendicular to gravity). As shown in Fig. 5(d), we clamped the helix and perform the experiment in a glycerol bath. During the experiments, we imaged the deformed shape of the helix using a digital camera. In Section 6.3, we measured the displacement of the free-end as a function of the applied field. The total length L and the concentration ratio c were varied as $L = 74, 81, 103$ mm and $c = 10, 20\%$, respectively, while the diameter $d = 2$ mm, the radius of natural curvature $R = 10$ mm and the pitch angle $\psi = 1.51$ rad were fixed. In Section 7, the deformation of the magnetic helix were studied, varying the pitch angle ψ and total length L in the range of $\psi = 1.26$–1.49 rad and $L = 65$–140 mm, while $d = 2$ mm, $R = 10$ mm, and $c = 20\%$ were kept fixed throughout Section 7.

6. Validation of the theory of hard magnetic rods vs experiments

In this section, we will use precision experiments on specific test configurations to perform a detailed validation of the theoretical framework introduced in Section 3.3 for hard MRE rods. In Sections 6.1 and 6.2, the twist instabilities for a straight rod and a helix are investigated under a constant field. Given that $\boldsymbol{p}_{\mathrm{mag}} = 0$ under the constant field, we can show that the magneto-elastic torque $\boldsymbol{q}_{\mathrm{mag}}$ in both naturally straight and curved configurations captures the corresponding experimental results in excellent agreement. Then, in Section 6.3, we study the deformation of a helix under a constant gradient field to test the validity of both $\boldsymbol{p}_{\mathrm{mag}}$ and $\boldsymbol{q}_{\mathrm{mag}}$.

6.1. Twist instability of a straight magnetic rod under magnetic loading

Consider a straight rod aligned with $\hat{\boldsymbol{e}}_x$ (clamped at $s = 0$), that is magnetized normal to the centerline tangent, i.e., $\boldsymbol{B}^{\mathrm{r}} = B^r \hat{\boldsymbol{e}}_z$. We apply the constant flux density as $\boldsymbol{B}^{\mathrm{a}} = -B^a \hat{\boldsymbol{e}}_z$ (see Fig. 6(a)–(d)). Figs. 6(a) and (c) are photographs from the experiments of the rod cross-sections at their free-ends, parallel with y-z planes. Three-dimensional representations of the straight MRE rods obtained from the simulations are shown in Figs. 6(b) and (d). The rod remains straight when the magnitude of the applied field B^{a} is sufficiently small enough (Fig. 6(a) and (b)), whereas the rod twists, with the centerline still straight, above the critical flux density B^{a*}_{twist} (Fig. 6(c) and (d)). In the experiments, we measured the twist angle ϕ_L at $s = L$ by tracking the rotation angle of a nitinol rod embedded near the free-end perpendicular to the centerline (as shown by $\hat{n}(L)$ in Figs. 6(a) and (c)). In the simulation, we also measured ϕ_L by computing the rotation angle for one of the basis vectors of the Cosserat frame $\hat{\boldsymbol{d}}_1$. In Fig. 6(e), we superpose the experimental and numerical results of ϕ_L as a function of $B^{\mathrm{a}}/B^{\mathrm{a}*}_{\mathrm{twist}}$. The error bars in the experimental data correspond to the uncertainty in the setting of the angle of the clamp. Experimental and numerical results are in excellent agreement with each other across the full parameter range in $B^{\mathrm{a}}/B^{\mathrm{a}*}_{\mathrm{twist}}$.

We rationalize the experimental and numerical results using the magnetic Kirchhoff equations that we derived in Section 3.3 by the perturbation against the twist instability. Following Goriely and Tabor (1997), we expand the Cosserat frame with respect to the straight configuration $(\hat{\boldsymbol{d}}_1^{(0)}, \hat{\boldsymbol{d}}_2^{(0)}, \hat{\boldsymbol{d}}_3^{(0)}) = (\hat{\boldsymbol{e}}_y, \hat{\boldsymbol{e}}_z, \hat{\boldsymbol{e}}_x)$ as

$$\hat{\boldsymbol{d}}_a = (\delta_{ab} + \varepsilon_{abc}\alpha_c)\hat{\boldsymbol{d}}_b^{(0)}, \tag{50}$$

where $\varepsilon_{abc}\alpha_c$ is the asymmetric tensor and $\alpha_a = \alpha_a(s)$ $(a = 1, 2, 3)$ is the small (angular) perturbation parameter $\alpha_a \ll 1$. The coefficient $\varepsilon_{abc}\alpha_c$ enforces the orthogonality of $\hat{\boldsymbol{d}}_a$ $(a = 1, 2, 3)$ even up to the 1st order of the perturbation. Plugging the perturbed form of $\hat{\boldsymbol{d}}_a$, Eq. (50), into the kinematic equation, Eq. (1), (see Appendix B for details), we find

$$\alpha_a' = \Omega_a\,, \tag{51}$$

from which we conclude that α_a represents the infinitesimal rotation angle around $\hat{\boldsymbol{d}}_a$. Given that the rod is clamped at $s = 0$ and free at $s = L$, the corresponding boundary conditions are $\alpha_a(0) = 0$ and $\alpha_a'(L) = \Omega(L) = 0$. Furthermore, $\boldsymbol{p}_{\mathrm{mag}} = 0$ and thus $\boldsymbol{F}(s) = 0$. Substituting Eq. (50) into Eq. (25) and linearizing the result for α_a yields

$$EI\alpha_1'' = -\frac{AB^{\mathrm{r}}B^{\mathrm{a}}}{\mu_0}\alpha_1, \tag{52}$$

$$EI\alpha_2'' = 0, \tag{53}$$

$$GJ\alpha_3'' = -\frac{AB^{\mathrm{r}}B^{\mathrm{a}}}{\mu_0}\alpha_3. \tag{54}$$

Eqs. (52)–(54) are the governing equations for the infinitesimal rotation angles α_a along the rod. To determine the conditions for the existence of nontrivial solutions $(\alpha_a(s) \neq 0)$ for Eqs. (52)–(54), we will substitute $\alpha_a \propto \sin(\pi s/2L)$ $(a = 1, 2, 3)$, which satisfies the boundary conditions $\alpha_a(0) = \alpha_a'(L) = 0$, into Eqs. (52)–(54). Eq. (53) gives us the null amplitude $\alpha_2(s) = 0$, while Eqs. (52) and (54) are satisfied if $AB^{\mathrm{r}}B^{\mathrm{a}}/\mu_0 = EI(\pi/2L)^2$ or $AB^{\mathrm{r}}B^{\mathrm{a}}/\mu_0 = GJ(\pi/2L)^2$ hold, respectively. The smaller value of B^{a} derived here

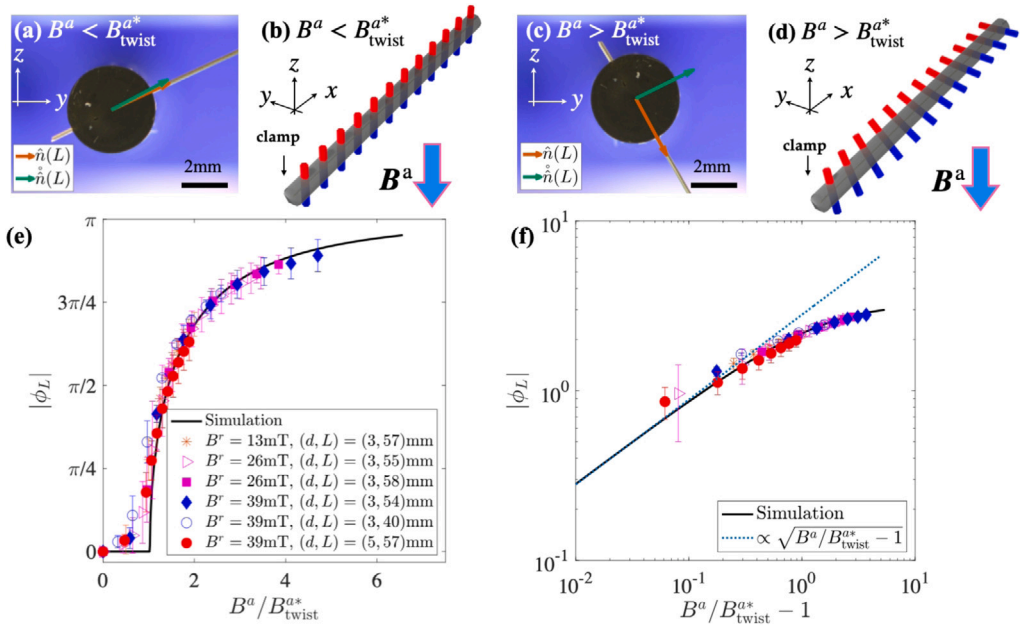

Fig. 6. Twist instability of straight MRE rods. (a) Experimental photograph of the cross section at $s = L$ with $B^{\text{a}} < B^{\text{a*}}_{\text{twist}}$. The symbols $\hat{n}(L)$ and $\mathring{\hat{n}}(L)$ represent the direction of the nitinol rod in the deformed and reference configuration, respectively. The corresponding simulation snapshot is shown in (b). (c) Experimental photograph of the cross section at $s = L$ with $B^{\text{a}} > B^{\text{a*}}_{\text{twist}}$. The corresponding simulation snapshot is shown in (d). (e) ϕ_L as a function of $B^{\text{a}}/B^{\text{a*}}_{\text{twist}}$. The data points are experimental results and the solid line is the simulation result. (f) Logarithmic plot of ϕ_L as a function of $B^{\text{a}}/B^{\text{a*}}_{\text{twist}} - 1$. The legend is the same as (e). The dashed line is the fitting of the power law with the exponent 1/2, Eq. (56), obtained through scaling arguments.

corresponds to the critical value of B^{a} for the twist instability, $B^{\text{a*}}_{\text{twist}}$. Since $GJ/EI = 1/(1+\nu) < 1$, the eigenvalue of Eq. (54) corresponds to the critical flux density, above which the rod twists: Hence, we find

$$B^{\text{a*}}_{\text{twist}} = \left(\frac{\pi}{2}\right)^2 \frac{\mu_0 GJ}{AB^{\text{r}}L^2}. \tag{55}$$

Notice that EI in Eq. (30) is now replaced by GJ in Eq. (55). Given that $\alpha_3 = \alpha_3(s)$ is the profile of the (infinitesimal) twisting angle (from Eq. (51)), $\alpha_3(L)$ corresponds to the twist angle of the free-end measured in our experiment and $\phi_L = \alpha_3(L)$ in the limit of $\phi_L \ll 1$. By analogy with the equation of clamped–free elastica (Audoly and Pomeau, 2010) (replacing $\alpha_3(s)$ with the bending angle in elastica), Eq. (54) is now mathematically equivalent to the amplitude equation for the pitch-fork bifurcation. In the neighborhood of $B^{\text{a}}/B^{\text{a*}}_{\text{twist}} \sim 1$, we thus anticipate that ϕ_L obeys the following scaling law, where the twist angle at the tip ϕ_L evolves as

$$\phi_L \propto \sqrt{\frac{B^{\text{a}}}{B^{\text{a*}}_{\text{twist}}} - 1}. \tag{56}$$

We find an excellent agreement between experiments and the theoretical description developed above ϕ_L, although the transition is not sharp due to the inevitable imperfection of the system below the critical field $B^{\text{a}}/B^{\text{a*}}_{\text{twist}} < 1$ (Strogatz, 2018). Furthermore, from the logarithmic plot in Fig. 6(f), we confirm that $|\phi_L|$ is consistent with the predicted scaling law Eq. (56), in the region of $|B^{\text{a}}/B^{\text{a*}}_{\text{twist}} - 1| \ll 1$. The above results demonstrate that our magnetic Kirchhoff equations correctly predict the twist instability of straight rods. In particular, we validated the magneto-elastic torque $\boldsymbol{q}_{\text{mag}}$ in the case of straight rods. Combining the fact that our framework reproduces the previous results on the planar deformation (Section 3.4) (Lum et al., 2016; Ciambella and Tomassetti, 2020; Wang et al., 2020; Yan et al., 2021) and the results presented in this subsection, the magnetic Kirchhoff equation (24) and (25) correctly predict the large deformation of naturally straight hard MRE rods. Next, we focus on the deformation of hard MRE rods that are naturally curved .

6.2. Buckling of a magnetic helix under constant field

We proceed by considering a naturally curved and twisted rod, i.e., a helix, which undergoes structural (buckling) instability of a helix at a critical field $B^{\text{a*}}$, but with an inevitable twist–bend coupling. We will show that our simulations and theoretical analyses rationalize our experimental results with excellent quantitative agreement.

We fabricate a hard magnetic helix with the pitch angle $\psi = 1.28$ rad, which is clamped such that the central axis is aligned along the coil axis $\hat{\boldsymbol{e}}_z$. We apply the magnetic field $\boldsymbol{B}^{\text{a}} = -B^{\text{a}}\hat{\boldsymbol{e}}_z$ on a helical rod with lengths in the range of $40 \le L$ [mm] ≤ 120. These helices are magnetized along their central axis as $\boldsymbol{B}^{\text{r}} = B^{\text{r}}\hat{\boldsymbol{e}}_z$. Below the critical field $B^{\text{a}} < B^{\text{a*}}$, the rod remains uniformly helical,

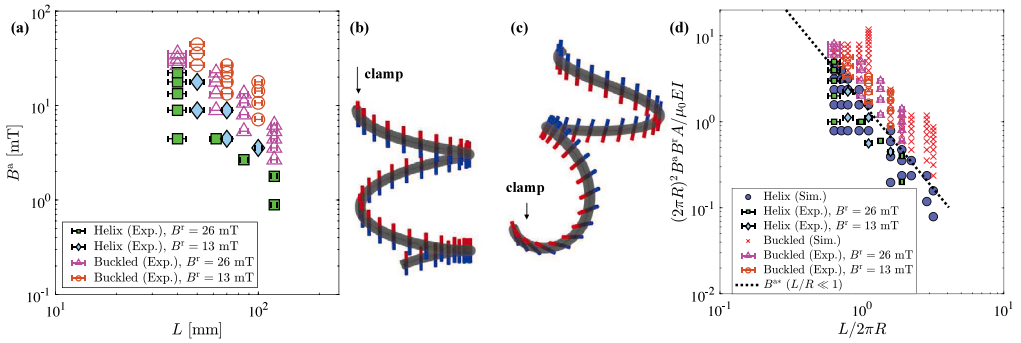

Fig. 7. Buckling of a magnetic helix. (a) Phase diagram of the buckling instability of a magnetic helix in experiments. Filled and empty data points are uniform or buckled helix states, respectively. Buckling of a magnetic helix under constant field. In the previous section. The dashed line is the analytic prediction in the limit of $L/R \ll 1$. The simulation snapshots for $L/R = 12$ correspond to $B^a/B^{a*} = 0.25$ (b) and $B^a/B^{a*} = 2.5$ (c). (d) Rescaled phase diagram of our experimental results. The simulation results and asymptotic solutions are superposed with $\psi = 1.28$ rad.

as shown in the filled data points in Fig. 7(a), buckling occurs when $B^a > B^{a*}$, as depicted by the open symbols. We regarded the rod as helical if the tip moves by less than the diameter d in the experiments.

We now specialize the magnetic Kirchhoff equations (24) and (25) for a magnetic helix to rationalize the experimental observations. The critical flux density for buckling of the magnetic helix B^{a*} can be derived via rigorous analysis of Eqs. (24) and (25). Here, to simplify the analysis and emphasize the importance of a twist–bend coupling in the system, we will compute the critical field strength B^{a*} in the limit of small curvature $KL \ll 1$ (K is total curvature for a helix defined later) but with $\psi < \pi/2$, which indeed provides a good prediction for our observations as we detail later.

Similarly to Section 6.1, we expand the Cosserat frame with respect to the uniform helix as we did in Eqs. (50) and (51). The Darboux vector in the uniform helix is $\boldsymbol{\Omega} = \kappa \hat{\boldsymbol{d}}_2 + \tau \hat{\boldsymbol{d}}_3$ with the natural curvature κ and twist τ. By integrating the kinematic relation Eq. (1), $\hat{\boldsymbol{d}}_a' = \boldsymbol{\Omega} \times \hat{\boldsymbol{d}}_a$, the Cosserat frame $\hat{\boldsymbol{d}}_a$ $(a = 1, 2, 3)$ for a helix in the reference configuration is computed as

$$\hat{\boldsymbol{d}}_1^{(0)}(s) = \cos(Ks)\hat{\boldsymbol{e}}_x - \sin(Ks)\hat{\boldsymbol{e}}_y, \tag{57}$$

$$\hat{\boldsymbol{d}}_2^{(0)}(s) = -\cos\psi\left(\sin(Ks)\hat{\boldsymbol{e}}_x + \cos(Ks)\hat{\boldsymbol{e}}_y\right) - \sin\psi\hat{\boldsymbol{e}}_z, \tag{58}$$

$$\hat{\boldsymbol{d}}_3^{(0)}(s) = \sin\psi\left(\sin(Ks)\hat{\boldsymbol{e}}_x + \cos(Ks)\hat{\boldsymbol{e}}_y\right) - \cos\psi\hat{\boldsymbol{e}}_z. \tag{59}$$

We choose the central axis to be parallel to $\hat{z}$ and define the pitch angle ψ as $\kappa = K\sin\psi$, $\tau = K\cos\psi$, and $K \equiv \sqrt{\kappa^2 + \tau^2}$. The radius of curvature on the x–y plane R and ψ are related as $\kappa = \sin^2\psi/R$ and $\tau = \sin 2\psi/2R$ (see Appendix C for the detailed derivation).

Plugging Eqs. (57)–(59) into the magnetic Kirchhoff equations (Eqs. (24) and (25)) and using Eqs. (50) and (51), we obtain the set of equilibrium equations for the linear perturbation of a helix in the limit of $KL \ll 1$:

$$EI\alpha_1'' = -\frac{AB^rB^a}{\mu_0}\alpha_1 \tag{60}$$

$$EI\alpha_2'' = \frac{AB^rB^a}{\mu_0}\cos\psi\left(\alpha_2\cos\psi - \alpha_3\sin\psi\right) \tag{61}$$

$$GJ\alpha_3'' = -\frac{AB^rB^a}{\mu_0}\sin\psi\left(\alpha_2\cos\psi - \alpha_3\sin\psi\right), \tag{62}$$

with boundary conditions that are the same as those given in Section 6.1: $\alpha_a(0) = \alpha_a'(L) = 0$. Eqs. (60)–(62) are the linearized moment balance equations of Eq. (25).

Assuming the functional form $\alpha_a \propto \sin(ks)$ with $k = \pi/2L$ (that satisfies the boundary conditions $\alpha_a(0) = \alpha_a'(L) = 0$), the critical magnetic field B^{a*} satisfying $\alpha_a \neq 0$ can be obtained from Eqs. (61) and (62) as

$$B^{a*} = \left(\frac{\pi}{2L}\right)^2 \frac{\mu_0}{AB^r}\frac{EI}{\cos^2\psi + (EI/GJ)\sin^2\psi}. \tag{63}$$

Eq. (63) captures the previous results on planar bending in Eq. (30) in Section 3.4, as well as the twist instabilities in Eq. (55), which we investigated in Section 6.1. Indeed, by taking the limit $\psi \to 0$, (i.e., rod clamped vertically and magnetized along the centerline tangent), we get $B^{a*} \to B^{a*}_{\text{bend}}$. By contrast, in the limit of $\psi \to \pi/2$, (i.e., rod clamped horizontally but magnetized as in Section 6.1), we recover $B^{a*} \to B^{a*}_{\text{twist}}$. In a recent study (Barreto et al., 2021), a similar (but not identical) buckling condition was found for *paramagnetic rods*, as long as we identify their angle between inclusions and the centerline with our pitch angle ψ.

We performed numerical simulations corresponding to the buckling of a hard magnetic helix under the constant magnetic field. When the applied field is sufficiently small $B^a < B^{a*}$, the rod remains helical, but the helix buckles when $B^a > B^{a*}$. In Figs. 7(b) and (c), we show representative snapshots of the numerical simulations for $B^a < B^{a*}$ and $B^a > B^{a*}$, respectively. Based on Eq. (63), we summarize experimental and numerical results in the rescaled phase diagram shown in Fig. 7(d). In the simulations, we remark

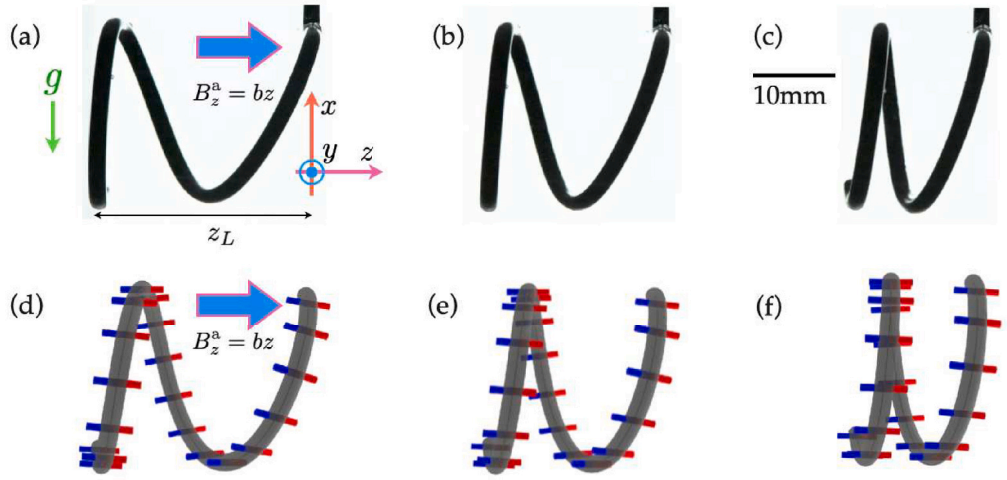

Fig. 8. Deformation of a hard magnetic helix. Snapshots of (a)–(c) experiments and (d)–(f) simulations with B^r = 13 mT, R = 10 mm and L = 103 mm. The corresponding values of rescaled gradient are (a) (d) $\lambda_m = 3.0$, (b) (e) $\lambda_m = 2.5$, (c) (f) $\lambda_m = 2.0$.

that the rod remains helical if the displacement of the free-end is less than $10^{-3}\ell_0$, where ℓ_0 is the natural length of the spring in the simulation (unit length of the simulation). The phase boundary between the undeformed (helical) and buckled states is in an excellent agreement between experiments and simulations. Furthermore, the analytic prediction (Eq. (63)) correctly predicts both experimental and numerical results. It should be noted that not only Eq. (63) predicts the phase boundary for $L/R \ll 1$, but also that for $L/R = O(1)$, without any adjustable parameters. A more rigorous analysis will be able to derive the full analytic prediction of the phase boundary, wheres it is beyond the scope of the current paper.

In this subsection, we have confirmed that the magneto-elastic torque $\boldsymbol{q}_{\text{mag}}$ Eq. (22) derived in Section 3.1 correctly predicts the experimental results for a naturally curved and twisted rod. Combining the results from Section 6.1 and those in this subsection, we validated the magnetic Kirchhoff equations (Eqs. (24) and (25)) in three-dimensional deformation under the constant field. In the next subsection, we consider the case of loading in a constant gradient magnetic field to validate the distributed magneto-elastic force $\boldsymbol{p}_{\text{mag}}$ (Eq. (21)) to fully validate our theoretical framework.

6.3. *Deformation of a magnetic helix under constant gradient field*

In this subsection, we will validate the framework for magnetic helices under the *constant gradient* field ($\boldsymbol{p}_{\text{mag}}, \boldsymbol{q}_{\text{mag}} \neq 0$). For this third and final test configuration, the magnetic helix is clamped at $s = 0$, while setting the other end ($s = L$) to be free. As we increase the gradient of the field b (or equivalently, the rescaled gradient $\lambda_m = L/\ell_m$, see Eq. (34)), the magnetic helix stretches. We will present results on the displacement of the free-end as a function of λ_m and find excellent agreement between experiments and simulations. In this subsection, we study the magnetic helix of a pitch shorter than that in Section 6.2. Hence, the helix interacts with itself non-locally via long-range interaction. Although long-range interactions are not considered in our theory, we can predict the stretching of the helix as long as the pitch becomes larger upon increasing λ_m.

As an illustrative configuration, the magnetic helix is placed with its central axis is aligned with the coil axis, and the clamped-end is located on the $z = 0$ plane (see Fig. 8 for a photograph of the setup), within the error of ± 1 mm. The magnetic helix has geometries of $(L, R) = (10, 103)$ mm and pitch angle $\psi = 1.51$ rad. We suspend the magnetic helix in a glycerol bath, horizontally. The gradient of the magnetic field b is increased from zero up to $b = 1.06$ T/m (maximum value in our setup), and then b is decreased back to zero.

In the absence of the applied field, $\lambda_m = 0$ (i.e. $b = 0$), the helix is fully contracted due to the long-range dipole–dipole interaction. As discussed in Zhao et al. (2019), Yan et al. (2021) and Section 3, the applied field gradient is analogous to a unidirectional body force of constant magnitude such as gravity. Hence, the helix extends (or contracts) when λ_m is increased or decreased, respectively. We present the photograph of the extended helix with $\lambda_m = 3.0$ in Fig. 8(a). The rescaled gradient is then decreased to $\lambda_m = 2.5$ and $\lambda_m = 2.0$, as shown in Fig. 8(b) and (c), respectively. We performed the numerical simulations of the magnetic helix under the constant gradient field to compare its deformed configurations with the experimental ones. Figs. 8(d), (e) and (f) are the snapshots of our discrete simulation with $\lambda_m = 3.0, 2.5$ and 2.0, respectively. Similar to our experimental observations, the helix contracts as λ_m is decreased. The predicted shapes in the numerical simulation agree with the configurations in experiments qualitatively.

To quantify the deformation of the helix in the present configuration, we measured the end-to-end distance along z between the clamp and the tip of the helix: $z_L \equiv z(L) - z(0)$ defined in Fig. 8(a). In Fig. 9(a)–(c), we plot z_L as a function of the rescaled applied field gradient $\lambda_m = L/\ell_m$ for different values of L or B^r, where ℓ_m is the magneto-bending length defined in Eq. (34). The data points correspond to the experimental results. As an example, we describe the experimental results presented in Fig. 9(a). In

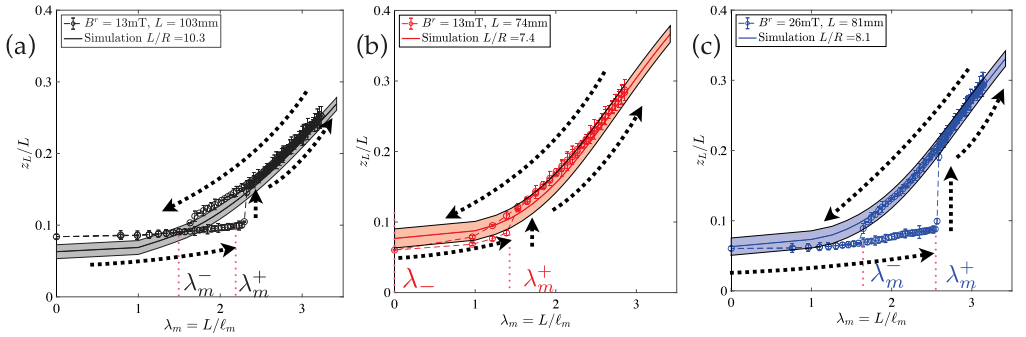

Fig. 9. The z-position of the free-end as a function of the rescaled gradient $\lambda_m = L/\ell_m$ for different B^r and length L. The data points and solid lines are experimental and simulation results, respectively. The shaded areas are errors due to the clamped position computed from the simulation. (a) $B^r = 13$ mT, $L = 103$ mm (b) $B^r = 13$ mT, $L = 74$ mm (c) $B^r = 26$ mT, $L = 81$ mm.

the absence of the applied field $\lambda_m = 0$, the helix is in self-contact due to long-range attractive interactions. Upon increasing λ_m, the helix loses self-contact when $\lambda_m = \lambda_m^+$. Past this point, z_L increases as the distributed magneto-elastic force stretches the helix. When λ_m is decreased, the helix contracts until self-contact at $\lambda_m = \lambda_m^-$. For the sake of convenience, we refer to the branch where the helix is in self-contact *self-contact branch*, and to the branch without self-contact as the *magneto-elastic branch*.

We find that the values of $\lambda_m^\pm$ depend on B^r and L. Indeed, in Figs. 9(a) and (c), $\lambda_m^- \neq 0$, while, in Fig. 9(b), $\lambda_m^- = 0$. The fact that $\lambda_m^- = 0$ implies that the helical shape (without contact) is stable but it is not a unique stable state due to the long-range interactions. The value of $\lambda_m^\pm$ can be used to classify the hysteric behavior, depending on the magnitude of residual flux density $|B^r|$, the pitch angle ψ, and the rescaled total length L/R. We will discuss the hysteric behavior in z_L more in detail, in Section 7.

Complementing the experimental data, we performed the discrete simulations corresponding to our experimental settings to measure the end-to-end distance z_L as a function of λ_m. Given that our theory does not include the self long-range interaction, z_L is not hysteretic (the self-contact branch does not appear). Still the predictions from our model are in excellent agreement with the experimental results in the magneto-elastic branches. In Figs. 9(a)–(c), we plot the predictions from the simulations as solid lines. The width of the shaded region in Figs. 9(a)–(c) correspond to the propagation of errors due to the ± 1 mm, uncertainty of the total length L measurement. From the excellent agreement between the experimental data and numerical results, we conclude that the magnetic Kirchhoff equations (Eqs. (24) and (25)) provide an accurate quantitative prediction for the deformation of the magnetic helix under a constant gradient field, when the self long-range interaction is not dominant.

In this section, we combined the discrete simulations with experiments, to validate the magnetic Kirchhoff equations (Eqs. (24) and (25)) derived in Section 3.3, for specific cases where the long-range interaction can be neglected compared with the distributed magneto-elastic forces. We showed that the numerical simulations can predict the behavior of the magneto-elastic branch observed experimentally. We have validated the magneto-elastic torque $\boldsymbol{q}_{\rm mag}$ and force $\boldsymbol{p}_{\rm mag}$ in a naturally straight and curved rod, thereby allowing us to validate Eqs. (24) and (25) in geometrically nonlinear deformations, at least when the long-range interaction is negligible. Next, in Section 7, we perform a more systematic experimental study of when and how the long-range interaction affects the deformation of a magnetic helix.

7. Limitations of the theory

In this section, we systematically quantify the limitation of the theory through precision experiments alone, because the self long-range interactions is not included in Eqs. (24) and (25); doing so is a challenging endeavor that goes beyond the scope of the present study. We classify the hysteretic behavior reported in Fig. 9 based on the value of $\lambda_m^\pm$; the critical field strength at which z_L jumps discontinuously. We will discuss the classification by considering the structural instability of the magnetic helix in the absence of the applied field, that is $\lambda_m = 0$.

The long-range interactions in the magnetic helix depend on the combined effects of the magnitude of the magnetization $|\mathcal{M}| \propto |\boldsymbol{B}^r|$ and the geometry of the helix (e.g., the pitch angle ψ and the rescaled total length $L/(2\pi R)$). The magnitude of the magnetization $|\mathcal{M}|$ is programmed at the fabrication stage by the concentration ratio of the NdPrFeB particles c. When c is small, the long-range interaction will be suppressed (and vice versa). On the other hand, the dependence of ψ and $L/(2\pi R)$ is highly nontrivial, as we discuss below.

The constant gradient field is applied to the magnetic helix as in Section 6.3. The helix is extended and contracted under the constant gradient magnetic field, for several pitch angles (in the natural configuration). We introduce the normalized pitch angle as $\tilde{\psi} \equiv \psi/(\pi/2)$ such that $\tilde{\psi} = 1$ corresponds to the planar circle with zero twist (experimentally non-realizable due to the finite diameter of the rod) and $\tilde{\psi} = 0$ corresponds to a straight rod. As $\tilde{\psi}$ decreases, the pitch of the helix increases. Practically, $\tilde{\psi}_{\rm max} = 0.96$ is the largest value of $\tilde{\psi}$ realizable in our experimental conditions with $(d, R) = (2, 10)$ mm. Our rods are fabricated systematically through the procedure in Section 5.1 with different pitch angles in the range $0.80 \leq \tilde{\psi} \leq 0.95$. We clamp the magnetized helix with $B^r = 26$ mT at $z(0) = 0$, while $s = L$ is set to be free. Through the cyclic protocols consisting of increasing and decreasing the flux density, the values of λ_m characterizing the hysteresis $\lambda_m^\pm$ are identified (see Fig. 9 for the definition of $\lambda_m^\pm$).

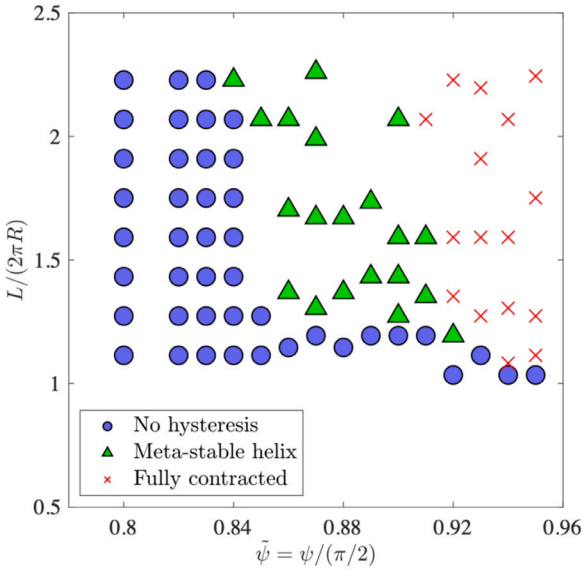

Fig. 10. Classification of the hysteretic behavior in the stretching and contraction of a magnetic helix. The phase diagram of hysteresis is obtained from experiments with $B^r = 26$ mT and $R = 10$ mm; ○: No hysteresis ($\lambda_m^+, \lambda_m^- = 0$), △: Meta-stable helix ($\lambda_m^+ \neq 0,\ \lambda_m^- = 0$) and ×: Fully contracted helix ($\lambda_m^+, \lambda_m^- \neq 0$).

In Fig. 10, we present the experimental phase diagram in the $\tilde{\psi}$-$L/2\pi R$ parameter space to classify the response against λ_m, finding that there are three different possible responses (i)–(iii), depending on the geometry of the magnetic helix. (i) When $L/2\pi R \simeq 1$ (length of the helix is nearly a single turn) or $\tilde{\psi}$ is small, (i.e. when the pitch $p = 2\pi R/\tan\psi$ is long enough), no hysteresis is observed (circles in Fig. 10). When we plot z_L as a function of λ_m, z_L changes continuously and reversibly for any λ_m. The tip of the helix follows the same curve upon increasing or decreasing λ_m. In this case, we have $\lambda_m^+ = \lambda_m^- = 0$ (Fig. 10). For higher values of ψ, we observe hysteresis, which is divided into two further categories; $\lambda_m^+ \neq 0,\ \lambda_m^- = 0$ or $\lambda_m^+, \lambda_m^- \neq 0$, which are shown as triangles and cross marks in Fig. 10, respectively. (ii) In the case of $\lambda_m^+ \neq 0,\ \lambda_m^- = 0$, z_L changes discontinuously from the contracted helix to the stretched helix at $\lambda_m = \lambda_m^+$, while z_L decreases smoothly as $\lambda_m \to 0$, i.e. $\lambda_m^- = 0$ (see Fig. 9(b) for the corresponding behavior). (iii) By contrast, in the case of $\lambda_m^+, \lambda_m^- \neq 0$, z_L jumps at both λ_m^+ and λ_m^-. Thus, if we plot z_L as a function of λ_m, we obtain similar curves as those in Figs. 9 (a) and (c).

The classification of the hysteretic responses in the z_L-λ_m plots (i)–(iii) can be understood by considering the configuration at $\lambda_m = 0$. In the following, we discuss the stability of the uniform helix at $\lambda_m = 0$ against mechanical perturbations. (i) When $\lambda_m^+ = \lambda_m^- = 0$ (no hysteresis), the uniform helical shape corresponds to a unique energy minimum. The reference configuration is mono-stable upon any mechanical perturbations, because self-interactions have minimal effects. (ii) For $\lambda_m^+ \neq 0$ and $\lambda_m^- = 0$, the uniform helix is stable but it is not a unique minimum. In this case, the helix can contracts to the (stable) state with the normalized pitch angle of $\tilde{\psi} = \tilde{\psi}_{\max}$ if perturbed; we call this state *meta-stable helix*. Lastly, (iii) for $\lambda_m^+, \lambda_m^- \neq 0$, the uniform helix is no longer stable. Indeed, the contracted state is the unique energy minimum. In this third case, the helix remains fully-contracted against any mechanical perturbation.

The nature of the hysteretic behavior in magnetic helices depends on the concentration ratio of NdPrFeB particles c and the geometry of the helix as described by ψ and $L/(2\pi R)$. We classified the deformation due to long-range self-interactions based on the value of λ_m at which $z_L(\lambda_m)$ changes discontinuously. The hysteretic behavior in the magnetic helix originates from the bi-stability due to the long-range interactions. In the previous sections, we had validated the magnetic Kirchhoff rod equations when the long-range interaction can be neglected. At the same time, we clarified the limitation of our theory systematically. The hysteretic behavior, which our theory cannot capture, is observed only when the pitch angle $\tilde{\psi}$ is large and when the rod is long $L/(2\pi R) \gtrsim 1$. We can conclude that the magnetic Kirchhoff rod equations (Eqs. (24) and (25)) are valid as long as ψ, $L/(2\pi R)$, or c remains small.

8. Conclusion

The goal of the present study was to develop a Kirchhoff-like theory for hard magnetic rods based on dimensional reduction. Our theoretical framework, rooted in three-dimensional elasticity, yielded a reduced (centerline-based) description of the magnetic rod (Section 3). The set of governing equations contain magneto-elastic forces and torques (Eqs. (21) and (22)), in addition to the purely elastic ones for a (non-magnetic) rod. We validated the magnetic Kirchhoff rod equations (Eqs. (24) and (25)) through a set of precision experiments. Our theoretical results supplemented by the discrete simulation are in excellent agreement with the experimental results. Moreover, the magnetic Kirchhoff rod equations reproduce the previous results on the planar deformation of hard magnetic beams or elastica (Lum et al., 2016; Zhao et al., 2019; Yan et al., 2021; Ciambella and Tomassetti, 2020). We

confirmed that the force and moment balance equations in our theory for hard magnetic rods reduce to those of Lum et al. (2016), Zhao et al. (2019), Yan et al. (2021), Ciambella and Tomassetti (2020) for beams and elastica.

To validate our theory for the three-dimensional deformation of magnetic rods, we performed three different sets of experiments; (i) a straight magnetic rod under constant external magnetic field (Section 6.1), (ii) a helical rod under constant field (Section 6.2), and (iii) a helical rod under the constant gradient field (Section 6.3), with the clamped–free boundary conditions. (i) In the case of a straight rod under the constant field, we studied the twist instability. When the rod is magnetized along $\hat{\boldsymbol{d}}_1$ (perpendicular to the centerline tangent $\hat{\boldsymbol{d}}_3$) and we apply an anti-parallel field, the rod twists, while its centerline remains straight. We derived an analytical prediction for the critical applied field for this twist instability B^{a*}_{twist}, which is in excellent agreement with experimental results. (ii) We studied the buckling instability of a helical rod under constant external magnetic field. The helix was magnetized along its central axis. When we apply the field to the magnetic helix, it buckles above the critical applied field B^{a*}. We showed that this instability is triggered by a balance between elastic and magneto-elastic torques. The critical applied fields were predicted analytically from a linear stability analysis. The simulation results correctly capture the experimental observations. (iii) Under a constant gradient field, the helix magnetized along the central axis stretches (or contracts) as we increase (or decrease) the applied field strength. Due to the long-range self-interaction between magnetic dipoles within the rod, the deformation is hysteretic upon extension and contraction.

Our framework correctly predicts the deformation of the magnetic helix when its pitch is large enough or when the long-range self-interactions are negligible. The hysteretic behavior was studied systematically through experiments by controlling the pitch angle ψ of the helix. We revealed that there are three types of behavior; no hysteresis state, meta-stable, and fully contracted helices, depending on the total length L/R and the pitch angle ψ.

Although our theory is in excellent agreement with the experimental results when the distributed magneto-elastic force and torque are dominant, the non-local interactions between the magnetization vectors $\boldsymbol{\mathcal{M}}$ are necessary to describe the hysteretic behavior. In Hall et al. (2013), Vella et al. (2014), Schönke and Fried (2017), the continuum mechanics of *magnetic chains* has been studied by considering the self-interactions between magnetic beads. In the future, combining the continuum mechanics of the magnetic dipole interactions and our magnetic Kirchhoff rod equations, the hysteretic behavior of the magnetic helix could be studied in detail theoretically. Extending the magnetic Kirchhoff equations to include the dipole–dipole interactions is one of the interesting directions of future works. Also, extending our theoretical framework toward dynamics of hard magnetic rods is also another exciting opportunity for future work. The dynamics could be simulated by considering the (external) viscous force and torque of a surrounding medium in Eqs. (24) and (25).

The framework established in this paper would be valuable to simulate the large deformation of hard magnetic rods used in micro or soft-robotics (Diller et al., 2014; Tsumori et al., 2015; Huang et al., 2016; Ciambella and Tomassetti, 2020) or haptic devices (Pece et al., 2017). In the future, novel functional devices of complex geometries could be developed by combining the simple building blocks studied in this paper.

CRediT authorship contribution statement

Tomohiko G. Sano: Conceptualization, Methodology, Validation, Investigation, Formal analysis, Software, Writing – original draft, Writing – review & editing. **Matteo Pezzulla:** Conceptualization, Methodology, Validation, Investigation, Writing – original draft, Writing – review & editing. **Pedro M. Reis:** Conceptualization, Methodology, Supervision, Writing – review & editing.

Declaration of competing interest

The authors declare that they have no known competing financial interests or personal relationships that could have appeared to influence the work reported in this paper.

Acknowledgments

T.G.S. was supported by Grants-in-Aid for Japan Society for the Promotion of Science Overseas Research Fellowship 2019-60059 and MEXT KAKENHI 18K13519.

Appendix A. Elastic forces in the discrete simulations

In this Appendix, we derive expressions for the elastic forces used in our simulations, following previous work. To simplify the indices for the discrete formulation, we rewrite the basis of the Cosserat frame as $(\hat{\boldsymbol{f}}_i, \hat{\boldsymbol{v}}_i, \hat{\boldsymbol{u}}_i)$, instead of $(\hat{\boldsymbol{d}}_{1,i}, \hat{\boldsymbol{d}}_{2,i}, \hat{\boldsymbol{d}}_{3,i})$. This Appendix is structured as follows. In Appendix A.1, we derive expressions for the elastic bending and twisting forces and torques. The inextensibility conditions for the centerline is ensured, approximately, by introducing elastic springs between adjacent nodes, the details of which are provided in Appendix A.2.

A.1. Elastic bending and twisting

In this subsection, we derive the elastic bending and twisting forces and torque used in the discrete simulations. First, in Appendix A.1.1, we derive the (discrete) relation between adjacent Cosserat frames, using Euler angles. The discretization of the kinematic relation follows in Appendix A.1.2, where the Darboux vector is rewritten with respect to the Euler angles. In Appendix A.1.3, we express the variation of the discretized elastic rod energy with respect to the variation of the Euler angles. Finally, in Appendix A.1.4, we write the variation of the Euler angles with the set of the variation of position of the node and the infinitesimal angle $(\delta \boldsymbol{r}_i, \delta \chi_{3,i})$.

A.1.1. Euler Angles and Cosserat frames

At each node i $(i = 1, \dots, N)$, we express the Cosserat frame as

$$\begin{aligned}\mathbf{D}_i &= (\hat{\boldsymbol{f}}_i, \hat{\boldsymbol{v}}_i, \hat{\boldsymbol{u}}_i),\\ &= \begin{pmatrix} \hat{f}_{i,x} & \hat{v}_{i,x} & \hat{u}_{i,x} \\ \hat{f}_{i,y} & \hat{v}_{i,y} & \hat{u}_{i,y} \\ \hat{f}_{i,z} & \hat{v}_{i,z} & \hat{u}_{i,z} \end{pmatrix}\end{aligned} \tag{A.1}$$

where the tangent vector between adjacent nodes is denoted by $\hat{\boldsymbol{u}}_i \equiv (\boldsymbol{r}_{i+1} - \boldsymbol{r}_i)/|\boldsymbol{r}_{i+1} - \boldsymbol{r}_i|$. We seek to relate the two Cosserat frames $\mathbf{D}_i$ and $\mathbf{D}_{i+1}$ via rigid body rotations. In general, two orthogonal basis in three dimensions can be identical by combining rigid body transformation and three sequential rotations (Goldstein et al., 2002), whose angles are called the Euler angles. The protocol for the rotations is as follows:

- **Step 1:** We define the nodal line $\hat{\mathcal{N}}$ as $\hat{\mathcal{N}} \equiv \hat{\boldsymbol{u}}_i \times \hat{\boldsymbol{u}}_{i+1}/|\hat{\boldsymbol{u}}_i \times \hat{\boldsymbol{u}}_{i+1}|$. Then, the Cosserat frame $\mathbf{D}_i$ rotates by an angle α_i around $\hat{\boldsymbol{u}}_i$ so that $\hat{\boldsymbol{f}}_i$ coincides with $\hat{\mathcal{N}}$. We label the quantities after the Step 1 with the superscript $(\cdot)^{(1)}$.
- **Step 2:** We rotate $\mathbf{D}_i^{(1)}$ by an angle β_i around the nodal line $\hat{\mathcal{N}}$ so that $\hat{\boldsymbol{u}}_i^{(1)} (= \hat{\boldsymbol{u}}_i)$ coincides with $\hat{\boldsymbol{u}}_{i+1}$. The quantities after Step 2 are labeled with the superscript $(\cdot)^{(2)}$.
- **Step 3:** After Step 2, the two-dimensional coordinates $\hat{\boldsymbol{f}}_i^{(2)}$-$\hat{\boldsymbol{v}}_i^{(2)}$ and $\hat{\boldsymbol{f}}_{i+1}$-$\hat{\boldsymbol{v}}_{i+1}$ share the same plane (because $= \hat{\boldsymbol{u}}_i^{(2)}$ and $\hat{\boldsymbol{u}}_{i+1}$ coincide). Finally, we rotate $\mathbf{D}_i^{(2)}$ by an angle γ_i around $\hat{\boldsymbol{u}}_{i+1}$, such that $\hat{\boldsymbol{f}}_i^{(2)}$ and $\hat{\boldsymbol{f}}_{i+1}$ are identical.

Therefore, the Cosserat frames at the ith and the $(i+1)$th nodes can be related via the following linear relations, using the set of angles $(\alpha_i, \beta_i, \gamma_i)$.

$$\mathbf{D}_{i+1} = \mathbf{D}_i R(\alpha_i, \beta_i, \gamma_i), \tag{A.2}$$

where the rotation matrix R is

$$\begin{aligned} R(\alpha,\beta,\gamma) &= \begin{pmatrix} \cos\alpha & -\sin\alpha & 0 \\ \sin\alpha & \cos\alpha & 0 \\ 0 & 0 & 1 \end{pmatrix} \begin{pmatrix} \cos\beta & 0 & \sin\beta \\ 0 & 1 & 0 \\ -\sin\beta & 0 & \cos\beta \end{pmatrix} \begin{pmatrix} \cos\gamma & -\sin\gamma & 0 \\ \sin\gamma & \cos\gamma & 0 \\ 0 & 0 & 1 \end{pmatrix} \\ &= \begin{pmatrix} \cos\alpha\cos\beta\cos\gamma - \sin\alpha\sin\gamma & -\cos\alpha\cos\beta\sin\gamma - \sin\alpha\cos\gamma & \cos\alpha\sin\beta \\ \sin\alpha\cos\beta\cos\gamma + \cos\alpha\sin\gamma & -\sin\alpha\cos\beta\sin\gamma + \cos\alpha\cos\gamma & \sin\alpha\sin\beta \\ -\sin\beta\cos\gamma & \sin\beta\sin\gamma & \cos\beta \end{pmatrix} \end{aligned} \tag{A.3}$$

With the above transformation rule and the set of Euler angles $(\alpha_i, \beta_i, \gamma_i)$, the frame $(\hat{\boldsymbol{f}}_{i+1}, \hat{\boldsymbol{v}}_{i+1}, \hat{\boldsymbol{u}}_{i+1})$ can be linearly related to $(\hat{\boldsymbol{f}}_i, \hat{\boldsymbol{v}}_i, \hat{\boldsymbol{u}}_i)$.

Above, we showed the geometric relation between $\mathbf{D}_i$ and $\mathbf{D}_{i+1}$ by using the Euler angles, $(\alpha_i, \beta_i, \gamma_i)$. Next, we express the Darboux vectors using these Euler angles.

A.1.2. Discretization of kinematic relations

We seek to express the components of the Darboux vectors, Ω_a $(a = 1, 2, 3)$, with respect to the Euler angles $(\alpha_i, \beta_i, \gamma_i)$. From the kinematic relation for the Cosserat frame, Eq. (1), we find

$$\Omega_1 = -\hat{\boldsymbol{d}}_2 \cdot \hat{\boldsymbol{d}}_3', \quad \Omega_2 = \hat{\boldsymbol{d}}_3' \cdot \hat{\boldsymbol{d}}_1, \quad \Omega_3 = \hat{\boldsymbol{d}}_1' \cdot \hat{\boldsymbol{d}}_2 \tag{A.4}$$

Although there are a few options for the discretization of Eq. (1) (Chirico and Langowski, 1994), we adopt the following:

$$\Omega_{1,i} \simeq -\frac{\hat{\boldsymbol{u}}_{i+1} \cdot \hat{\boldsymbol{v}}_i}{\ell_0}, \quad \Omega_{2,i} \simeq \frac{\hat{\boldsymbol{u}}_{i+1} \cdot \hat{\boldsymbol{f}}_i}{\ell_0}, \quad \Omega_{3,i} \simeq \frac{\hat{\boldsymbol{f}}_{i+1} \cdot \hat{\boldsymbol{v}}_i}{\ell_0}. \tag{A.5}$$

As a reminder, the natural length of the spring between adjacent nodes is represented by ℓ_0. Hence, using the geometric relations obtained from Eq. (A.2), we get

$$\Omega_{1,i} = -\frac{1}{\ell_0} \sin\beta_i \sin\alpha_i \simeq -\frac{1}{\ell_0} \beta_i \sin\alpha_i \tag{A.6}$$

$$\Omega_{2,i} = \frac{1}{\ell_0} \sin\beta_i \cos\alpha_i \simeq \frac{1}{\ell_0} \beta_i \cos\alpha_i \tag{A.7}$$

$$\Omega_{3,i} = \frac{1}{\ell_0}\sin(\alpha_i+\gamma_i) \simeq \frac{\alpha_i+\gamma_i}{\ell_0}. \tag{A.8}$$

To obtain Eqs. (A.6)–(A.8), we have assumed $|\beta_i| \ll 1$ and $|\alpha_i+\gamma_i| \ll 1$ given that the total curvature $\sqrt{\Omega_1^2+\Omega_2^2}$ and the magnitude of twist $|\Omega_3|$ are small in our system (Hookean model). So far, we have expressed Ω_a with respect to Euler angles:

$$\Omega_{a,i} = \Omega_{a,i}(\alpha_i,\beta_i,\gamma_i). \tag{A.9}$$

Thus, we can also rewrite $E_{\rm el}$ as a function of $(\alpha_i,\beta_i,\gamma_i)$ as

$$E_{\rm el} \simeq \sum_i E_i(\alpha_i,\beta_i,\gamma_i). \tag{A.10}$$

The discretized elastic force and torques can then be computed from the variation of $E_{\rm el}$, as

$$\delta E_{\rm el} = -\sum_i \boldsymbol{F}_{{\rm bt},i}\cdot\delta\boldsymbol{r}_i - \sum_i T_i\delta\chi_{3,i}. \tag{A.11}$$

Here, $\boldsymbol{F}_{{\rm bt},i}$ and T_i are the sum of elastic bending and twisting forces and the elastic torque acting on ith node, respectively. To compute $\boldsymbol{F}_{{\rm bt},i}$ and T_i we need to express the variations of the Euler angles, $\delta\alpha_i,\delta\beta_i$ and $\delta\gamma_i$ with respect to $\delta\boldsymbol{r}_i$ and $\delta\chi_{3,i}$, which is the final task detailed in the remaining two sections, below.

A.1.3. Relation between the constitutive law and Euler angles

We consider the elastic energy density at node i, $E_i(\alpha_i,\beta_i,\gamma_i)$, defined as $E_{\rm el} \simeq \sum_i E_i(\alpha_i,\beta_i,\gamma_i)$, whose variation defines the discretized version of the moment $M_{a,i}$ as

$$\delta E_i = \sum_{a=1,2,3} M_{a,i}\delta\Omega_{a,i}, \tag{A.12}$$

$$M_{1,i} = \ell_0 EI(\Omega_{1,i}-\mathring{\Omega}_{1i}) \tag{A.13}$$

$$M_{2,i} = \ell_0 EI(\Omega_{2,i}-\mathring{\Omega}_{2i}) \tag{A.14}$$

$$M_{3,i} = \ell_0 GJ(\Omega_{3,i}-\mathring{\Omega}_{3i}). \tag{A.15}$$

Here, with the aid of Eqs. (A.6)–(A.8), all of $M_{a,i}$ are already expressed with the Euler angles. The variation of $\Omega_{a,i}$, $\delta\Omega_{a,i}$, can be expressed with the Euler angles (see Eqs. (A.6)–(A.8)). To compute δE_i, the variation of the Darboux vector $\delta\Omega_{a,i}$ needs to be written as a function of the Euler angles. Using Eqs. (A.6)–(A.8), we get

$$\delta\Omega_{1,i} = \frac{\delta\beta_i}{\beta_i}\Omega_{1,i} - \delta\alpha_i\Omega_{2,i}, \quad \delta\Omega_{2,i} = \frac{\delta\beta_i}{\beta_i}\Omega_{2,i} + \delta\alpha_i\Omega_{1,i}, \quad \ell_0\delta\Omega_{3,i} = \delta(\alpha_i+\gamma_i). \tag{A.16}$$

The variation of the elastic energy density at node i, δE_i, can now be written as a function of the Euler angles:

$$\begin{aligned}\delta E_i &= M_{1,i}\delta\Omega_{1,i} + M_{2,i}\delta\Omega_{2,i} + M_{3,i}\delta\Omega_{3,i}\\ &= P_i\delta\beta_i + Q_i\delta\alpha_i + R_i\delta(\alpha_i+\gamma_i),\end{aligned} \tag{A.17}$$

where we have defined the following three quantities P_i, Q_i and R_i to simplify the notation:

$$P_i = \frac{M_{1,i}\Omega_{1,i} + M_{2,i}\Omega_{2,i}}{\beta_i}, \tag{A.18}$$

$$Q_i = -M_{1,i}\Omega_{2,i} + M_{2,i}\Omega_{1,i}, \tag{A.19}$$

$$R_i = \frac{M_{3,i}}{\ell_0}. \tag{A.20}$$

The final task is to rewrite $\delta\beta_i$ and $\delta(\alpha_i\pm\gamma_i)$ as a function of $\delta\boldsymbol{r}_i$ and $\delta\chi_{3,i}$.

A.1.4. Variation of Euler angles

Finally, we show that the variation of the Euler angles can be expressed with respect to $\delta\boldsymbol{r}_i$ and $\delta\chi_{3,i}$. We recall that $\hat{\boldsymbol{u}}_i$ is the tangent vector of the relative positions between adjacent nodes; $\hat{\boldsymbol{u}}_i = (\boldsymbol{r}_{i+1}-\hat{\boldsymbol{r}}_i)/\ell_i$ with $\ell_i \equiv |\boldsymbol{r}_{i+1}-\hat{\boldsymbol{r}}_i|$, whose variations are solely written with respect to the set of $\delta\boldsymbol{r}_i$ and $\delta\boldsymbol{r}_{i+1}$. The variation of $\delta\chi_{3,i}$ is associated with that of $\hat{\boldsymbol{f}}_i$ and $\hat{\boldsymbol{v}}_i$:

$$\delta\chi_{3,i} = \delta\hat{\boldsymbol{f}}_i\cdot\hat{\boldsymbol{v}}_i = -\delta\hat{\boldsymbol{v}}_i\cdot\hat{\boldsymbol{f}}_i \tag{A.21}$$

We notice that $\delta\hat{\boldsymbol{f}}_i$ and $\delta\hat{\boldsymbol{v}}_i$ are, respectively, normal to $\hat{\boldsymbol{f}}_i$ and $\hat{\boldsymbol{v}}_i$ because the latter two are unit vectors; $\hat{\boldsymbol{f}}_i\cdot\hat{\boldsymbol{f}}_i = \hat{\boldsymbol{v}}_i\cdot\hat{\boldsymbol{v}}_i = 1$. Expanding $\delta\hat{\boldsymbol{f}}_i$ and $\delta\hat{\boldsymbol{v}}_i$ on the corresponding two dimensional planes and using (A.21), yields

$$\begin{aligned}\delta\hat{\boldsymbol{f}}_i &= (\delta\hat{\boldsymbol{f}}_i\cdot\hat{\boldsymbol{u}}_i)\hat{\boldsymbol{u}}_i + (\delta\hat{\boldsymbol{f}}_i\cdot\hat{\boldsymbol{v}}_i)\hat{\boldsymbol{v}}_i\\ &= -(\hat{\boldsymbol{f}}_i\cdot\delta\hat{\boldsymbol{u}}_i)\hat{\boldsymbol{u}}_i + \delta\chi_{3,i}\hat{\boldsymbol{v}}_i.\end{aligned} \tag{A.22}$$

and

$$\delta\hat{\boldsymbol{v}}_i = (\delta\hat{\boldsymbol{v}}_i\cdot\hat{\boldsymbol{u}}_i)\hat{\boldsymbol{u}}_i + (\delta\hat{\boldsymbol{v}}_i\cdot\hat{\boldsymbol{f}}_i)\hat{\boldsymbol{f}}_i$$

$$= -(\hat{\boldsymbol{v}}_i \cdot \delta\hat{\boldsymbol{u}}_i)\hat{\boldsymbol{u}}_i - \delta\chi_{3,i}\hat{\boldsymbol{f}}_i. \tag{A.23}$$

Given that $\delta\hat{\boldsymbol{u}}_i$ is written as a function of $\delta\boldsymbol{r}_i$, we find that only $\delta\boldsymbol{r}_i$ and $\delta\chi_{3,i}$ appear (not $\delta\chi_{1,i}$ and $\delta\chi_{2,i}$) in Eqs. (A.22) and (A.23). As such, we expect that the variation of the Euler angles will be expressed with respect to the set of $(\delta\boldsymbol{r}_i, \delta\chi_{3,i})$, requiring us to solve (A.2) in terms of α_i, β_i and γ_i. Specifically, we express $\cos\beta_i$, $\sin(\alpha_i \pm \gamma_i)$ and $\cos(\alpha_i \pm \gamma_i)$ as functions of the inner products between the Cosserat frame basis vectors of i and ith nodes. Given that this calculation is cumbersome, we provide only the final results,

$$\delta(\alpha_i \pm \gamma_i) = \pm\delta(\chi_{3,i+1} \mp \chi_{3,i}) + \boldsymbol{A}_i^{\pm} \cdot \delta\boldsymbol{r}_{i+2} + (\boldsymbol{B}_i^{\pm} - \boldsymbol{A}_i^{\pm}) \cdot \delta\boldsymbol{r}_{i+1} - \boldsymbol{B}_i^{\pm} \cdot \delta\boldsymbol{r}_i \tag{A.24}$$

$$\delta\beta_i = -\boldsymbol{D}_i^{+} \cdot \delta\boldsymbol{r}_{i+2} - (\boldsymbol{D}_i^{-} - \boldsymbol{D}_i^{+}) \cdot \delta\boldsymbol{r}_{i+1} + \boldsymbol{D}_i^{-} \cdot \delta\boldsymbol{r}_i, \tag{A.25}$$

where we have introduced the following vector quantities to simplify the notation:

$$\boldsymbol{D}_i^{+} = \frac{\sin\beta_i\hat{\boldsymbol{u}}_i - \cos\beta_i(\cos\alpha_i\hat{\boldsymbol{f}}_i + \sin\alpha_i\hat{\boldsymbol{v}}_i)}{\ell_{i+1}}, \quad \boldsymbol{D}_i^{-} = \frac{\cos\alpha_i\hat{\boldsymbol{f}}_i + \sin\alpha_i\hat{\boldsymbol{v}}_i}{\ell_i}, \tag{A.26}$$

$$\boldsymbol{A}_i^{+} = \frac{1}{\ell_{i+1}}\frac{(\hat{\boldsymbol{v}}_{i+1}\cdot\hat{\boldsymbol{u}}_i)\hat{\boldsymbol{f}}_{i+1} - (\hat{\boldsymbol{f}}_{i+1}\cdot\hat{\boldsymbol{u}}_i)\hat{\boldsymbol{v}}_{i+1}}{1+\hat{\boldsymbol{u}}_{i+1}\cdot\hat{\boldsymbol{u}}_i}, \quad \boldsymbol{B}_i^{+} = \frac{1}{\ell_i}\frac{(\hat{\boldsymbol{u}}_{i+1}\cdot\hat{\boldsymbol{f}}_i)\hat{\boldsymbol{v}}_i - (\hat{\boldsymbol{u}}_{i+1}\cdot\hat{\boldsymbol{v}}_i)\hat{\boldsymbol{f}}_i}{1+\hat{\boldsymbol{u}}_{i+1}\cdot\hat{\boldsymbol{u}}_i}, \tag{A.27}$$

$$\boldsymbol{A}_i^{-} = \frac{1}{\ell_{i+1}}\frac{(\hat{\boldsymbol{v}}_{i+1}\cdot\hat{\boldsymbol{u}}_i)\hat{\boldsymbol{f}}_{i+1} - (\hat{\boldsymbol{f}}_{i+1}\cdot\hat{\boldsymbol{u}}_i)\hat{\boldsymbol{v}}_{i+1}}{1-\hat{\boldsymbol{u}}_{i+1}\cdot\hat{\boldsymbol{u}}_i}, \quad \boldsymbol{B}_i^{-} = \frac{1}{\ell_i}\frac{(\hat{\boldsymbol{u}}_{i+1}\cdot\hat{\boldsymbol{v}}_i)\hat{\boldsymbol{f}}_i - (\hat{\boldsymbol{u}}_{i+1}\cdot\hat{\boldsymbol{f}}_i)\hat{\boldsymbol{v}}_i}{1-\hat{\boldsymbol{u}}_{i+1}\cdot\hat{\boldsymbol{u}}_i}. \tag{A.28}$$

When computing $\boldsymbol{A}_i^{-}$ and $\boldsymbol{B}_i^{-}$, one needs to ensure that the denominators do not vanish. We have introduced a small cut-off number to avoid such numerical artifacts. Substituting Eqs. (A.24) and (A.25) into (A.17) and arranging the indices i, we can finally express $\delta E_{\rm el}$ with respect to $\delta\boldsymbol{r}_i$ and $\delta\chi_{3,i}$ as (A.11), to obtain the discrete version of the elastic bending and twisting force and axial torque. Note here that only the infinitesimal rotation angle $\delta\chi_{3,i}$ is used to compute $\boldsymbol{F}_{{\rm bt},i}$ and T_i, not the angular parameter φ_i or $\chi_{3,i}$. This fact guarantees that the introduction of the angle parameter φ_i as Eq. (36) is not problematic, since φ_i, itself, is never used.

A.2. Elastic stretching forces

In the previous section, we derived the expressions for the elastic bending and twisting loads used in the discrete simulations. To ensure the inextensibility conditions for the centerline, approximatively, elastic linear springs are implemented between adjacent nodes, as $E_{\rm s} = \sum_i (k_s/2)|\boldsymbol{r}_{i+1} - \boldsymbol{r}_i|^2$ (Chirico and Langowski, 1994), where the value of stiffness was chosen to be $k_s = (64/\pi)(EI\ell_0^3/d^4)$. Given that the energetic cost for stretch is still much larger than for bending or twisting, the variations of the distance between neighboring nodes become smaller than 1% of ℓ_0 (natural length of the spring). Thus, the inextensibility of the centerline is realized approximately. Similarly to the previous section, through variational calculus, we obtain the elastic stretching force at the ith node, $\boldsymbol{F}_{s,i}$, as

$$\delta E_{\rm s} = -\sum_i \boldsymbol{F}_{{\rm s},i} \cdot \delta\boldsymbol{r}_i. \tag{A.29}$$

The sum of $\boldsymbol{F}_{{\rm bt},i}$ and $\boldsymbol{F}_{{\rm s},i}$ represents the elastic contribution in the equation of motion used of the discrete simulations (see Eq. (46)); $\boldsymbol{f}_i = \boldsymbol{F}_{{\rm bt},i} + \boldsymbol{F}_{{\rm s},i}$.

Appendix B. Derivation of Eq. (51)

In this Appendix, we provide the detailed derivation of Eq. (51);

$$\alpha_a' = \Omega_a\,. \tag{B.1}$$

We recall that our rod is naturally curved and twisted: $\boldsymbol{\Omega}^{(0)} = \Omega_a^{(0)}\hat{\boldsymbol{d}}_a^{(0)}$. We expand the Cosserat frame basis in Eq. (50) around the reference configuration $\hat{\boldsymbol{d}}_a^{(0)}$. We will determine the relationship between the first-order perturbation of the components of the Darboux vector $\Omega_a^{(1)}$ defined as

$$\Omega_a = \Omega_a^{(0)} + \Omega_a^{(1)} + \cdots\,, \tag{B.2}$$

and the first order perturbation of $\hat{\boldsymbol{d}}_a$, α_a. Note that $\Omega_a^{(1)}$ and α_a are infinitesimal quantities of the same order $\Omega_a^{(1)} \sim \alpha_a$. We substitute Eqs. (50)

$$\hat{\boldsymbol{d}}_a = (\delta_{ab} + \varepsilon_{abc}\alpha_c)\hat{\boldsymbol{d}}_b^{(0)}\,, \tag{B.3}$$

and (B.2) into Eq. (1); $\hat{\boldsymbol{d}}_a' = \boldsymbol{\Omega}\times\hat{\boldsymbol{d}}_a$, to derive Eq. (51). The final result is consistent with that in Goriely and Tabor (1997) (which is based on matrix representation), while our derivation is based on a tensor representation.

First, the kinematic equation (1) is rewritten using the Eddington epsilon as

$$\hat{\boldsymbol{d}}_a' = -\varepsilon_{abc}\Omega_b\hat{\boldsymbol{d}}_c, \tag{B.4}$$

which also holds for the base solution as $\hat{\boldsymbol{d}}_a^{(0)\prime} = -\varepsilon_{abc}\Omega_b^{(0)}\hat{\boldsymbol{d}}_c^{(0)}$. The left-hand side of Eq. (B.4) is computed as

$$\hat{\boldsymbol{d}}_a' = \{(\delta_{ab} + \varepsilon_{abc}\alpha_c)\hat{\boldsymbol{d}}_b^{(0)}\}'$$

$$
\begin{aligned}
&= -\varepsilon_{abc}\Omega_b^{(0)}\hat{\boldsymbol{d}}_c^{(0)} + \varepsilon_{abc}\alpha_c'\hat{\boldsymbol{d}}_b^{(0)} - \varepsilon_{abc}\varepsilon_{bde}\alpha_c\Omega_d^{(0)}\hat{\boldsymbol{d}}_e^{(0)} \\
&= -\varepsilon_{abc}\Omega_b^{(0)}\hat{\boldsymbol{d}}_c^{(0)} + \varepsilon_{abc}\alpha_c'\hat{\boldsymbol{d}}_b^{(0)} - (\delta_{cd}\delta_{ae} - \delta_{ce}\delta_{ad})\alpha_c\Omega_d^{(0)}\hat{\boldsymbol{d}}_e^{(0)} \\
&= -\varepsilon_{abc}\Omega_b^{(0)}\hat{\boldsymbol{d}}_c^{(0)} + \varepsilon_{abc}\alpha_c'\hat{\boldsymbol{d}}_b^{(0)} - (\alpha_c\Omega_c^{(0)})\hat{\boldsymbol{d}}_a^{(0)} + \Omega_a^{(0)}(\alpha_c\hat{\boldsymbol{d}}_c^{(0)}).
\end{aligned} \tag{B.5}
$$

We expand the right-hand side of Eq. (B.4) as

$$
\begin{aligned}
-\varepsilon_{abc}\Omega_b\hat{\boldsymbol{d}}_c &= -\varepsilon_{abc}(\Omega_b^{(0)} + \Omega_b^{(1)})(\delta_{cd} + \varepsilon_{cde}\alpha_e)\hat{\boldsymbol{d}}_d^{(0)} \\
&= -\varepsilon_{abc}\Omega_b^{(0)}\hat{\boldsymbol{d}}_c^{(0)} - \varepsilon_{abc}\Omega_b^{(1)}\hat{\boldsymbol{d}}_c^{(0)} - \varepsilon_{abc}\varepsilon_{cde}\alpha_e\Omega_b^{(0)}\hat{\boldsymbol{d}}_d^{(0)} \\
&= -\varepsilon_{abc}\Omega_b^{(0)}\hat{\boldsymbol{d}}_c^{(0)} - \varepsilon_{abc}\Omega_b^{(1)}\hat{\boldsymbol{d}}_c^{(0)} - (\delta_{ad}\delta_{be} - \delta_{ae}\delta_{bd})\alpha_e\Omega_b^{(0)}\hat{\boldsymbol{d}}_d^{(0)} \\
&= -\varepsilon_{abc}\Omega_b^{(0)}\hat{\boldsymbol{d}}_c^{(0)} - \varepsilon_{abc}\Omega_b^{(1)}\hat{\boldsymbol{d}}_c^{(0)} - (\alpha_c\Omega_c^{(0)})\hat{\boldsymbol{d}}_a^{(0)} + \alpha_a(\Omega_c^{(0)}\hat{\boldsymbol{d}}_c^{(0)}).
\end{aligned} \tag{B.6}
$$

Note that, in Eqs. (B.5) and (B.6), we dropped higher order terms (e.g. the terms proportional to $\alpha_a\Omega_b^{(1)}$).

Substituting Eqs. (B.5) and (B.6) into Eq. (B.4), we obtain the tensorial relation

$$
\varepsilon_{abc}\alpha_c'\hat{\boldsymbol{d}}_b^{(0)} = -\varepsilon_{abc}\Omega_b^{(1)}\hat{\boldsymbol{d}}_c^{(0)} + \alpha_a(\Omega_c^{(0)}\hat{\boldsymbol{d}}_c^{(0)}) - \Omega_a^{(0)}(\alpha_c\hat{\boldsymbol{d}}_c^{(0)}). \tag{B.7}
$$

Next, by taking the inner product between Eq. (B.7) and $\hat{\boldsymbol{d}}_d^{(0)}$, and by arranging the indices, we arrive at

$$
\varepsilon_{abc}\alpha_c' = \varepsilon_{abc}\Omega_c^{(1)} + \left(\alpha_a\Omega_b^{(0)} - \Omega_a^{(0)}\alpha_b\right). \tag{B.8}
$$

The presence of the term inside the parenthesis in the right-hand side of Eq. (B.8) encodes the geometric non-linearity intrinsic to a naturally curved rod. When the rod is naturally straight, $\Omega_a^{(0)} = 0$, we recover Eq. (51).

Appendix C. Derivation of Eqs. (57) –(59)

In this Appendix, we derive the Cosserat frame basis for the uniform helix Eqs. (57)–(59). To do so, we will integrate the kinematic relation Eq. (1) with $\boldsymbol{\Omega} = \kappa\hat{\boldsymbol{d}}_2 + \tau\hat{\boldsymbol{d}}_3$. The goal is to express $\boldsymbol{r}(s)$ and $\hat{\boldsymbol{d}}_a$ $(a = 1, 2, 3)$ in terms of the Cartesian basis $\hat{\boldsymbol{e}}_i$. From the kinematic relation, we get

$$
\hat{\boldsymbol{d}}_1' = -\kappa\hat{\boldsymbol{d}}_3 + \tau\hat{\boldsymbol{d}}_2, \tag{C.1}
$$

$$
\hat{\boldsymbol{d}}_2' = -\tau\hat{\boldsymbol{d}}_1, \tag{C.2}
$$

$$
\hat{\boldsymbol{d}}_3' = \kappa\hat{\boldsymbol{d}}_1, \tag{C.3}
$$

which are the same as the Frenet–Serret equations (Audoly and Pomeau, 2010). Differentiating Eq. (C.1) with respect to s, and with the help of Eqs. (C.2) and (C.3), we find the ODE only for $\hat{\boldsymbol{d}}_1$;

$$
\hat{\boldsymbol{d}}_1'' = -K^2\hat{\boldsymbol{d}}_1\,. \tag{C.4}
$$

Here, we introduced the normalized curvature K as $K = \sqrt{\kappa^2 + \tau^2}$, or equivalently

$$
\kappa = K\sin\psi, \quad \tau = K\cos\psi. \tag{C.5}
$$

After integrating Eq. (C.4) twice, we compute $\hat{\boldsymbol{d}}_1$ as

$$
\hat{\boldsymbol{d}}_1(s) = \cos(Ks)\hat{\boldsymbol{d}}_1(0) + \frac{\tau}{K}\sin(Ks)\hat{\boldsymbol{d}}_2(0) - \frac{\kappa}{K}\sin(Ks)\hat{\boldsymbol{d}}_3(0). \tag{C.6}
$$

Following a similar procedure for $\hat{\boldsymbol{d}}_2$ and $\hat{\boldsymbol{d}}_3$, we obtain

$$
\hat{\boldsymbol{d}}_2(s) - \hat{\boldsymbol{d}}_2(0) = -\frac{\tau}{K}\sin(Ks)\hat{\boldsymbol{d}}_1(0) - \frac{\tau}{K^2}(1 - \cos(Ks))(\tau\hat{\boldsymbol{d}}_2(0) - \kappa\hat{\boldsymbol{d}}_3(0)), \tag{C.7}
$$

$$
\hat{\boldsymbol{d}}_3(s) - \hat{\boldsymbol{d}}_3(0) = \frac{\kappa}{K}\sin(Ks)\hat{\boldsymbol{d}}_1(0) + \frac{\kappa}{K^2}(1 - \cos(Ks))(\tau\hat{\boldsymbol{d}}_2(0) - \kappa\hat{\boldsymbol{d}}_3(0)). \tag{C.8}
$$

By integrating $\boldsymbol{r}' = \hat{\boldsymbol{d}}_3$, the centerline position is obtained as

$$
\boldsymbol{r}(s) - \boldsymbol{r}(0) = \frac{\kappa}{K^2}(1 - \cos(Ks))\hat{\boldsymbol{d}}_1(0) - \frac{\kappa}{K^3}\sin(Ks)(\tau\hat{\boldsymbol{d}}_2(0) - \kappa\hat{\boldsymbol{d}}_3(0)) + \frac{\tau s}{K^2}(\kappa\hat{\boldsymbol{d}}_2(0) + \tau\hat{\boldsymbol{d}}_3(0)), \tag{C.9}
$$

where the unit vector of the central axis of the helix $\hat{N}$ is

$$
\hat{N} \equiv \frac{\kappa}{K}\hat{\boldsymbol{d}}_2(0) + \frac{\tau}{K}\hat{\boldsymbol{d}}_3(0). \tag{C.10}
$$

Finally, let us rewrite Eq. (C.9) in a more compact form by choosing $\hat{\boldsymbol{d}}_a(0)$ and $\boldsymbol{r}(0)$ such that the central axis lies along $-\hat{\boldsymbol{e}}_z$; i.e., we select $\hat{N} = -\hat{\boldsymbol{e}}_z$, $\hat{\boldsymbol{d}}_1(0) = \hat{\boldsymbol{e}}_x$, and $\hat{\boldsymbol{e}}_y = \hat{\boldsymbol{e}}_z \times \hat{\boldsymbol{e}}_x = -(\tau\hat{\boldsymbol{d}}_2(0) - \kappa\hat{\boldsymbol{d}}_3(0))/K$. Then, using Eq. (C.5), the centerline position is calculated as

$$
\boldsymbol{r}(s) = -\frac{\sin\psi}{K}\cos(Ks)\hat{\boldsymbol{e}}_x + \frac{\sin\psi}{K}\sin(Ks)\hat{\boldsymbol{e}}_y - s\cos\psi\hat{\boldsymbol{e}}_z, \tag{C.11}
$$

which implies

$$R = \frac{\sin\psi}{K}. \tag{C.12}$$

The normalized curvature K is now rewritten as a function of κ and ψ only; $K = \kappa\sqrt{1+\tan^{-2}\psi} = \kappa/\sin\psi$, i.e. $\kappa = \sin^2\psi/R$ and $\tau = \sin\psi\cos\psi/R = \sin 2\psi/2R$. The choice of $\hat{N}$ allows us to obtain the Cosserat frame basis vectors as

$$\hat{\boldsymbol{d}}_1(s) = \cos(Ks)\hat{\boldsymbol{e}}_x - \sin(Ks)\hat{\boldsymbol{e}}_y, \tag{C.13}$$

$$\hat{\boldsymbol{d}}_2(s) = -\cos\psi\left(\sin(Ks)\hat{\boldsymbol{e}}_x + \cos(Ks)\hat{\boldsymbol{e}}_y\right) - \sin\psi\hat{\boldsymbol{e}}_z, \tag{C.14}$$

$$\hat{\boldsymbol{d}}_3(s) = \sin\psi\left(\sin(Ks)\hat{\boldsymbol{e}}_x + \cos(Ks)\hat{\boldsymbol{e}}_y\right) - \cos\psi\hat{\boldsymbol{e}}_z, \tag{C.15}$$

thereby reproducing Eqs. (57)–(59) that we set out to derive.

References

Alapan, Y., Karacakol, A.C., Guzelhan, S.N., Isik, I., Sitti, M., 2020. Reprogrammable shape morphing of magnetic soft machines. Sci. Adv. 6 (38), eabc6414.

Audoly, B., Pomeau, Y., 2010. Elasticity and Geometry. Oxford Univ. Press.

Barreto, D.D., Saxena, S., Kumar, A., 2021. A magnetoelastic theory for kirchhoff rods having uniformly distributed paramagnetic inclusions and its buckling. Int. J. Solids Struct. (ISSN: 00207683) 111147. http://dx.doi.org/10.1016/j.ijsolstr.2021.111147.

Bergou, M., Wardetzky, M., Robinson, S., Audoly, B., Grinspun, E., 2008. Discrete elastic rods. In: ACM SIGGRAPH 2008 Papers. ACM Press, New York, New York, USA, p. 1.

Bigoni, D., 2015. Extremely Deformable Structures (CISM Lecture Notes No. 562). Springer-Verlag.

Brazier, L.G., 1927. On the flexure of thin cylindrical shells and other "thin" sections. Proc. R. Soc. Lond. Ser. A Contain. Pap. Math. Phys. Character 116 (773), 104–114.

Cebers, A., 2003. Dynamics of a chain of magnetic particles connected with elastic linkers. J. Phys.: Condens. Matter 15 (15), S1335–S1344.

Cēbers, A., Cīrulis, T., 2007. Magnetic elastica. Phys. Rev. E 76, 031504.

Cēbers, A., Javaitis, I., 2004. Bending of flexible magnetic rods. Phys. Rev. E 70, 021404.

Chen, T., Pauly, M., Reis, P.M., 2021. A reprogrammable mechanical metamaterial with stable memory. Nature 589 (7842), 386–390.

Chirico, G., Langowski, J., 1994. Kinetics of DNA supercoiling studied by Brownian dynamics simulation. Biopolymers 34 (3), 415–433.

Ciambella, J., Favata, A., Tomassetti, G., 2018. A nonlinear theory for fibre-reinforced magneto-elastic rods. Proc. R. Soc. Lond. A Math. Phys. Eng. Sci. 474 (2209), 20170703.

Ciambella, J., Tomassetti, G., 2020. A form-finding strategy for magneto-elastic actuators. Int. J. Non-Linear Mech. 119, 103297.

Counto, U.J., 1964. The effect of the elastic modulus of the aggregate on the elastic modulus, creep and creep recovery of concrete. Mag. Concr. Res. 16 (48), 129–138.

Danas, K., Kankanala, S.V., Triantafyllidis, N., 2012. Experiments and modeling of iron-particle-filled magnetorheological elastomers. J. Mech. Phys. Solids 60 (1), 120–138.

Dill, E.H., 1992. *Kirchhoff's* theory of rods. Arch. Hist. Exact Sci. 44 (1), 1–23.

Diller, E., Zhuang, J., Lum, G.Z., Edwards, M.R., Sitti, M., 2014. Continuously distributed magnetization profile for millimeter-scale elastomeric undulatory swimming. Appl. Phys. Lett. 104 (17), 174101.

Doedel, E., 1981. AUTO: a program for the automatic bifurcation analysis of autonomous systems. Congr. Numer. 30 (265).

Dorfmann, A., Ogden, R.W., 2003. Magnetoelastic modelling of elastomers. Eur. J. Mech. A Solids 22 (4), 497–507.

Dorfmann, L., Ogden, R.W., 2014. Nonlinear Theory of Electroelastic and Magnetoelastic Interactions. Springer, New York.

Dreyfus, R., Baudry, J., Roper, M.L., Fermigier, M., Stone, H.A., Bibette, J., 2005. Microscopic artificial swimmers. Nature 437 (7060), 862–865.

Garcia-Gonzalez, D., Hossain, M., 2021. Microstructural modelling of hard-magnetic soft materials: Dipole–dipole interactions versus zeeman effect. Extrem. Mech. Lett. (ISSN: 2352-4316) 48, 101382. http://dx.doi.org/10.1016/j.eml.2021.101382.

Gerbal, F., Wang, Y., Lyonnet, F., Bacri, J.-C., Hocquet, T., Devaud, M., 2015. A refined theory of magnetoelastic buckling matches experiments with ferromagnetic and superparamagnetic rods. Proc. Natl. Acad. Sci. 112 (23), 7135–7140.

Ginder, J.M., Nichols, M.E., Elie, L.D., Tardiff, J.L., 1999. Magnetorheological elastomers: properties and applications. In: Wuttig, M.R. (Ed.), Smart Structures and Materials 1999: Smart Materials Technologies. International Society for Optics and Photonics, pp. 131–138.

Goldstein, H., Poole Jr., C., Safko, J., 2002. Classical Mechanics, third ed. Addison-Wesley.

Goldstein, R.E., Powers, T.R., Wiggins, C.H., 1998. Viscous nonlinear dynamics of twist and writhe. Phys. Rev. Lett. (ISSN: 0031-9007) 80, http://dx.doi.org/10.1103/PhysRevLett.80.5232.

Goriely, A., 2017. The Mathematics and Mechanics of Biological Growth.

Goriely, A., Tabor, M., 1997. Nonlinear dynamics of filaments. III. Instabilities of helical rods. Proc. R. Soc. Lond. A Math. Phys. Eng. Sci. 453 (1967), 2583–2601.

Hairer, E., Nørsett, S.P., Wanner, G., 1993. Solving Ordinary Differential Equations I: Nonstiff Problems, second ed. Springer Verlag, Berlin.

Hall, C.L., Vella, D., Goriely, A., 2013. The mechanics of a chain or ring of spherical magnets. SIAM J. Appl. Math. 73 (6), 2029–2054.

Hu, W., Lum, G.Z., Mastrangeli, M., Sitti, M., 2018a. Small-scale soft-bodied robot with multimodal locomotion. Nature 554 (7690), 81–85.

Hu, N., Wang, L., Zhai, W., Sun, M., Xie, H., Wu, Z., He, Q., 2018b. Magnetically actuated rolling of star-shaped hydrogel microswimmer. Macromol. Chem. Phys. 219 (5), 1700540.

Huang, H.-W., Sakar, M.S., Riederer, K., Shamsudhin, N., Petruska, A., Pané, S., Nelson, B.J., Magnetic microrobots with addressable shape control, in: IEEE International Conference on Robotics and Automation ICRA Stockholm, Sweden, 2016.

Jackson, J.D., 1975. Classical Electrodynamics, second ed. Wiley, New York, NY.

Kim, Y., Yuk, H., Zhao, R., Chester, S.A., Zhao, X., 2018. Printing ferromagnetic domains for untethered fast-transforming soft materials. Nature 558 (7709), 274–279.

Landau, L.D., Lifshitz, E.M., 1980. Theory of Elasticity. Pergamon Press.

Li, W., Kostidis, K., Xianzhou Zhang, Yang Zhou, 2009. Development of a force sensor working with MR elastomers. In: 2009 IEEE/ASME International Conference on Advanced Intelligent Mechatronics. pp. 233–238. http://dx.doi.org/10.1109/AIM.2009.5230010.

Loukaides, E.G., Smoukov, S.K., Seffen, K.A., 2015. Magnetic actuation and transition shapes of a bistable spherical cap. Int. J. Smart Nano Mater. 5 (4), 270–282.

Lum, G.Z., Ye, Z., Dong, X., Marvi, H., Erin, O., Hu, W., Sitti, M., 2016. Shape-programmable magnetic soft matter. Proc. Natl. Acad. Sci. 113 (41), E6007–E6015.

Menzel, A.M., 2019. Mesoscopic characterization of magnetoelastic hybrid materials: magnetic gels and elastomers, their particle-scale description, and scale-bridging links. Arch. Appl. Mech. 89 (1), 17–45.

Moon, F.C., Pao, Y.-H., 1968. Magnetoelastic buckling of a thin plate. J. Appl. Mech. 35 (1), 53–58.

Morigaki, Y., Wada, H., Tanaka, Y., 2016. Stretching an elastic loop: Crease, helicoid, and pop out. Phys. Rev. Lett. 117 (19), 198003.
Pancaldi, L., Dirix, P., Fanelli, A., Lima, A.M., Stergiopulos, N., Mosimann, P.J., Ghezzi, D., Sakar, M.S., 2020. Flow driven robotic navigation of microengineered endovascular probes. Nature Commun. 11 (1), 1–14.
Pece, F., Zarate, J.J., Vechev, V., Besse, N., Gudozhnik, O., Shea, H., Hilliges, O., 2017. MagTics. In: UIST '17: The 30th Annual ACM Symposium on User Interface Software and Technology. ACM, New York, NY, USA, pp. 143–154.
Powers, T.R., 2010. Dynamics of filaments and membranes in a viscous fluid. Rev. Modern Phys. 82 (2), 1607–1631.
Psarra, E., Bodelot, L., Danas, K., 2019. Wrinkling to crinkling transitions and curvature localization in a magnetoelastic film bonded to a non-magnetic substrate. J. Mech. Phys. Solids 133, 103734.
Reichert, M., 2006. Hydrodynamic Interactions in Colloidal and Biological Systems (Ph.D. thesis). University Konstanz.
Rigbi, Z., Jilkén, L., 1983. The response of an elastomer filled with soft ferrite to mechanical and magnetic influences. J. Magn. Magn. Mater. 37 (3), 267–276.
Roper, M., Dreyfus, R., Baudry, J., Fermigier, M., Bibette, J., Stone, H.A., 2006. On the dynamics of magnetically driven elastic filaments. J. Fluid Mech. 554 (-1), 167–190.
Sano, T.G., Wada, H., 2018. Snap-buckling in asymmetrically constrained elastic strips. Phys. Rev. E 97 (1), 013002.
Sano, T.G., Wada, H., 2019. Twist-induced snapping in a bent elastic rod and ribbon. Phys. Rev. Lett. 122 (11), 114301.
Sano, T.G., Yamaguchi, T., Wada, H., 2017. Slip morphology of elastic strips on frictional rigid substrates. Phys. Rev. Lett. 118 (17), 178001.
Schmauch, M.M., Mishra, S.R., Evans, B.A., Velev, O.D., Tracy, J.B., 2017. Chained iron microparticles for directionally controlled actuation of soft robots. ACS Appl. Mater. Interfaces 9 (13), 11895–11901.
Schönke, J., Fried, E., 2017. Stability of vertical magnetic chains. Proc. R. Soc. Lond. A Math. Phys. Eng. Sci. 473 (2198), 20160703.
Seffen, K.A., Vidoli, S., 2016. Eversion of bistable shells under magnetic actuation: a model of nonlinear shapes. Smart Mater. Struct. 25 (6), 065010.
Singh, R.P., Onck, P.R., 2018. Magnetic field induced deformation and buckling of slender bodies. Int. J. Solids Struct. 143, 29–58.
Strogatz, S.H., 2018. Nonlinear Dynamics and Chaos: With Applications to Physics, Biology, Chemistry, and Engineering, second ed. CRC Press, Boca Raton, FL.
Tsumori, F., Saijou, A., Osada, T., Miura, H., 2015. Development of actuation system for artificial cilia with magnetic elastomer. Japan. J. Appl. Phys. 54 (6S1), 06FP12.
Vella, D., du Pontavice, E., Hall, C.L., Goriely, A., 2014. The magneto-elastica: from self-buckling to self-assembly. Proc. R. Soc. Lond. A Math. Phys. Eng. Sci. 470 (2162), 20130609.
Vogel, R., Stark, H., 2010. Force-extension curves of bacterial flagella. Eur. Phys. J. E 33 (3), 259–271.
Wada, H., Netz, R.R., 2007a. Model for self-propulsive helical filaments: Kink-pair propagation. Phys. Rev. Lett. 99 (10), 108102.
Wada, H., Netz, R.R., 2007b. Stretching helical nano-springs at finite temperature. Europhys. Lett. 77 (6), 68001.
Wang, C.Y., 1986. A critical review of the heavy elastica. Int. J. Mech. Sci. 28 (8), 549–559.
Wang, L., Kim, Y., Guo, C.F., Zhao, X., 2020. Hard-magnetic elastica. J. Mech. Phys. Solids 142, 104045.
Yan, D., Abbasi, A., Reis, P.M., 2021. A comprehensive framework for hard-magnetic beams: reduced-order theory, 3D simulations, and experiments. Int. J. Solids Struct. (ISSN: 00207683) 111319. http://dx.doi.org/10.1016/j.ijsolstr.2021.111319.
Yan, D., Pezzulla, M., Cruveiller, L., Abbasi, A., Reis, P.M., 2021b. Magneto-active elastic shells with tunable buckling strength. Nature Commun. 12 (1), 1–9.
Zhang, J., Diller, E., 2018. Untethered miniature soft robots: Modeling and design of a millimeter-scale swimming magnetic sheet. Soft Robot. 5 (6), 761–776.
Zhao, R., Kim, Y., Chester, S.A., Sharma, P., Zhao, X., 2019. Mechanics of hard-magnetic soft materials. J. Mech. Phys. Solids 124, 244–263.